

1 **Element release and reaction-induced porosity alteration during shale-hydraulic**
2 **fracturing fluid interactions**

3

4 Anna L. Harrison^{a,b*,1}, Adam D. Jew^{a,b}, Megan K. Dustin^a, Dana L. Thomas^a,
5 Claresta M. Joe-Wong^a, John R. Bargar^b, Natalie Johnson^c, Gordon E. Brown Jr.^{a,b,c}, and
6 Katharine Maher^a

7

8 ^aDepartment of Geological Sciences, 450 Serra Mall, Stanford University, Stanford, CA
9 94305, USA.

10

11 ^bStanford Synchrotron Radiation Lightsource, SLAC National Accelerator Laboratory,
12 2575 Sand Hill Road, Menlo Park, CA, 94025, USA.

13

14 ^cDepartment of Photon Science, SLAC National Accelerator Laboratory, 2575 Sand Hill
15 Road, Menlo Park, CA, 94025, USA

16

17 ¹Present address: Department of Earth Sciences, University College London, Gower
18 Street, London, WC1E 6BT, UK. *ALH - anna.harrison@ucl.ac.uk

19

20 *Corresponding author (phone: 1 650 723-2544; facsimile: 1 650 725-2199; e-mail:
21 anna.harrison@ucl.ac.uk).

22

23 **Abstract**

24 The use of hydraulic fracturing techniques to extract oil and gas from low
25 permeability shale reservoirs has increased significantly in recent years. During hydraulic
26 fracturing, large volumes of water, often acidic and oxic, are injected into shale
27 formations. This drives fluid-rock interaction that can release metal contaminants (*e.g.*,
28 U, Pb) and alter the permeability of the rock, impacting the transport and recovery of
29 water, hydrocarbons, and contaminants. To identify the key geochemical processes that
30 occur upon exposure of shales to hydraulic fracturing fluid, we investigated the chemical
31 interaction of hydraulic fracturing fluids with a variety of shales of different
32 mineralogical texture and composition. Batch reactor experiments revealed that the
33 dissolution of both pyrite and carbonate minerals occurred rapidly, releasing metal
34 contaminants and generating porosity. Oxidation of pyrite and aqueous Fe drove
35 precipitation of Fe(III)-(oxy)hydroxides that attenuated the release of these contaminants
36 via co-precipitation and/or adsorption. The precipitation of these (oxy)hydroxides
37 appeared to limit the extent of pyrite reaction. Enhanced removal of metals and
38 contaminants in reactors with higher fluid pH was inferred to reflect increased Fe-
39 (oxy)hydroxide precipitation associated with more rapid aqueous Fe(II) oxidation. The
40 precipitation of both Al- and Fe-bearing phases revealed the potential for the occlusion of
41 pores and fracture apertures, whereas the selective dissolution of calcite generated
42 porosity. These pore-scale alterations of shale texture and the cycling of contaminants
43 indicate that chemical interactions between shales and hydraulic fracturing fluids may
44 exert an important control on the efficiency of hydraulic fracturing operations and the
45 quality of water recovered at the surface.

46 **1. Introduction**

47 The extraction of oil and gas resources from low permeability shale reservoirs has
48 increased dramatically in recent years owing to the development and application of
49 horizontal drilling and hydraulic fracturing techniques (Kerr, 2010; U.S. Energy
50 Information Administration, 2013; Vidic et al., 2013). The development of these
51 resources has dramatically altered the energy landscape, particularly in the United States
52 (Kerr, 2010; U.S Energy Information Administration, 2013), which hosts numerous
53 economically viable shale oil and gas plays (Chermak and Schreiber, 2014; Vengosh et
54 al., 2013). However, hydraulic fracturing operations remain plagued by environmental
55 concerns, namely their potential to impact surface water and groundwater quality
56 (Brantley et al., 2014; Vengosh et al., 2013; Vidic et al., 2013). During hydraulic
57 fracturing operations, large volumes of fracturing fluids (*i.e.*, ~8-17 million liters;
58 Balashov et al., 2015; Chapman et al., 2012), that are often acidic and oxic (Stringfellow
59 et al., 2014), are injected into subsurface shale formations, resulting in a system that is
60 highly out of chemical equilibrium. It is hypothesized that disequilibrium between shale
61 and the hydraulic fracturing fluid will induce a myriad of reactions, including mineral
62 dissolution-precipitation, cation exchange, surface complexation, and oxidation-reduction
63 (redox) of solid and aqueous components. Such reactions may release harmful
64 contaminants into the environment (*e.g.*, U, Ra, As, Pb) (Balaba and Smart, 2012; Blauch
65 et al., 2009; Chermak and Schreiber, 2014; Vengosh et al., 2014; Vidic et al., 2013).
66 These chemical interactions may also alter the permeability and mechanical integrity of
67 the reservoir, influencing the efficiency of production and recovery of water for re-use.
68 Precipitation of secondary minerals and weakening and collapse of fractures due to

69 mineral dissolution could in part be responsible for the relatively inefficient production
70 experienced by many hydraulic fracturing operations (U.S. Energy Information
71 Administration, 2013). However, very little is currently known about the extent to which
72 chemical interactions between shales and these introduced fluids alter fluid and rock
73 properties, and whether these interactions occur on a timescale relevant to hydraulic
74 fracturing operations. Although monitoring of so-called flow-back and produced waters
75 (waters generated following fracturing and co-produced with hydrocarbons during well
76 operation, respectively) has revealed that the chemical composition of recovered waters
77 differs substantially from that of the injected fluid, the controls on the evolving
78 composition of the recovered fluids is not fully understood, and may reflect a
79 combination of factors including mixing of injected and formation fluids and fluid-rock
80 interaction (Barbot et al., 2013; Haluszczak et al., 2013; Lester et al., 2015; Orem et al.,
81 2014; Renock et al., 2016; Rowan et al., 2015; Shih et al., 2015; Ziemkiewicz and He,
82 2015; Zolfaghari et al., 2016). Experimental investigation is required to better define the
83 reactions that are likely to occur upon exposure of shales to hydraulic fracturing fluids
84 and their kinetics to assess the potential contribution of fluid-rock interaction to the
85 chemistry of produced waters and alteration of shale mechanical properties.

86 We investigated the types and relative rates of reactions occurring between shales
87 of different chemical and mineralogical compositions and a simulated hydraulic
88 fracturing fluid using a series of batch reactor experiments. Shale samples from four
89 different oil or gas shale reservoirs with unique mineralogical compositions were used,
90 including carbonate mineral-rich rocks from the Eagle Ford (South Texas) and Green
91 River (Colorado) formations, and comparatively carbonate mineral-poor rocks from the

92 Barnett (Central Texas) and Marcellus (New York) formations, all in the United States.
93 Currently, hydrocarbon production via hydraulic fracturing operations is ongoing for the
94 Eagle Ford, Barnett, and Marcellus formations. Green River shale is an oil-bearing
95 formation that, while not presently being exploited, has unique mineralogy that provides
96 an informative contrast to the other shales under investigation. The objectives of this
97 study were to: (1) identify the key geochemical reactions that occur upon exposure of oil
98 or gas-bearing shales to hydraulic fracturing fluids and their kinetics, (2) elucidate the
99 impact of initial shale mineralogy on the evolution of rock and fluid compositions during
100 hydraulic fracturing operations, (3) evaluate the potential for release of metal
101 contaminants to flowback and produced waters, and (4) assess reaction-induced
102 alterations of shale porosity. The evolution of fluid composition was tracked with time,
103 and the physical and chemical alteration of the shales was investigated post-reaction
104 using a combination of x-ray diffraction, x-ray fluorescence spectroscopy, and scanning
105 electron microscopy.

106

107 **2. Methods**

108 *2.1 Experimental methods*

109 The impacts of initial mineralogical composition and texture on the evolution of
110 shale reservoir geochemistry following injection of hydraulic fracturing fluid were
111 investigated using batch reactor experiments. A schematic of the experimental design and
112 further detail regarding experimental methods and analytical techniques are provided in
113 the Supporting Information (SI). Experiments were conducted for three weeks (referred
114 to as “short-term” experiments), three months (“intermediate-term”), and six months

115 (“long-term”). The short-term experiments were representative of the typical duration of
116 fluid injection for hydraulic fracturing, whereas the intermediate- and long-term
117 experiments were designed to investigate the interactions that may occur between the
118 shale reservoirs and unrecovered fracturing fluid over longer timescales after initial
119 fracturing operations are complete. In excess of 50% of the injected hydraulic fracturing
120 fluid is estimated to remain in the subsurface where it may continue to react with the rock
121 (Balashov et al., 2015; Roychaudhuri et al., 2013).

122 All experiments were conducted at Marcellus reservoir-representative
123 temperatures (80°C; Renock et al., 2016; Rowan et al., 2015) and circum-atmospheric
124 pressure in unstirred borosilicate glass serum vials. The use of circum-atmospheric rather
125 than reservoir pressures will cause minor differences in solubility between experimental
126 and field conditions, but the types of minerals that dissolve and their relative rates of
127 dissolution are not expected to be strongly impacted by differences in pressure.
128 Moreover, the impacts of pressure on solubility are small compared to temperature effects
129 (Morel and Herring, 1993). Shale samples from four different oil and/or gas-bearing
130 geological environments representing a wide range of clay and carbonate mineral
131 contents were exposed to simulated hydraulic fracturing fluid (SI Figure S1). These shale
132 samples included the Marcellus (M) gas shale (Oatka Creek Member, New York), the
133 Eagle Ford (EF) oil/gas shale (South Texas), the Barnett (B) gas shale (Central Texas),
134 and the Green River (GR) oil shale (Mahogany Ledge Member, Colorado). The GR and
135 M shales used were outcrop samples collected in August 2015, and July 2016,
136 respectively. EF and B samples were core samples taken at depth (3915 m and 2613 m,
137 respectively).

138 The initial chemical compositions of the shale samples were quantified using x-
139 ray fluorescence spectroscopy (XRF) by Jew et al. (*in press*) for the exact same GR, EF,
140 B, and M samples used in our experiments and are tabulated in Table 1. Semi-
141 quantitative analysis of initial mineralogical compositions was also conducted by Jew et
142 al. (*in press*) using x-ray diffraction (XRD) data (Table 2). Peak identification was
143 accomplished by matching the four most intense diffraction peaks for a given mineral to
144 diffraction patterns in the National Institute of Standards and Technology (NIST)
145 database. Semi-quantitative analysis was conducted by least squares fitting of the
146 diffraction patterns using the NIST diffraction pattern of reference compounds with the
147 software, JADE (Materials Data, 2002). Although these data are semi-quantitative, they
148 are in good agreement with previously reported mineralogical compositions for these
149 shales (Ali and Hascakir, 2015; Chalmers et al., 2012; Chermak and Schreiber, 2014).

150 For the purposes of this study, we separate the shales into “carbonate-rich” or
151 “carbonate-poor” categories depending on their mineralogical and chemical compositions
152 prior to reaction. Carbonate-rich shales contained >50 wt.% carbonate minerals, and
153 carbonate-poor shales contained <15 wt.% carbonate minerals. The Green River and
154 Eagle Ford samples are therefore designated carbonate-rich, and the Barnett and
155 Marcellus samples designated carbonate-poor. The composition of the simulated
156 fracturing fluid used in the experiments was formulated based on fluid compositions
157 typically employed in hydraulic fracturing operations conducted in the Marcellus shale,
158 and mimics that used in the National Energy Technology Laboratory's Marcellus Well E
159 in Greene County, PA (“FracFocus,” 2016; Hammack et al., 2014). It contained 99.78
160 wt.% MilliQ distilled, de-ionized water, 0.13 wt.% hydrochloric acid, 0.03 wt.% guar

161 gum, 0.02 wt.% ethylene glycol, 0.02 wt.% kerosene, 0.02 wt.% polyethylene glycol,
162 5.07×10^{-4} wt.% 2-ethylhexanol, and 1.73×10^{-4} wt.% glycol ether. During hydraulic
163 fracturing operations, all additives are not added simultaneously, but follow a specific
164 sequence. The experimental fluid represents a mixture of the relative proportions of these
165 in a single solution. The initial fluid had a pH of 2.0 and was assumed to be at
166 equilibrium with laboratory pO_2 (~ 0.21 atm), consistent with the injection of surface
167 waters during hydraulic fracturing operations. A major difference between the
168 experimental fluids and field conditions is that fluids in the field tend to have much
169 higher total dissolved solids (TDS). A high TDS fluid was not used in the experiments for
170 a number of reasons. First, high initial concentrations of anions like SO_4^{2-} and cations like
171 Mg and Ca make it difficult to accurately assess changes in aqueous concentrations due
172 to dissolution-precipitation reactions, and to conduct mass balance calculations to assess
173 the cycling of elements in the reactors. Second, a high TDS fluid may itself alter the rate
174 of mineral dissolution-precipitation reactions compared to published rate data from
175 laboratory experiments conducted at more moderate TDS. This complicates the direct
176 assessment of the impact of the hydraulic fracturing fluid additives on these mineral
177 dissolution-precipitation reactions, as deviations from published data could be due to the
178 high TDS rather than the fracture fluid additives. In addition, high TDS complicates the
179 calculation of aqueous speciation. Finally, fracturing fluids are injected into shale
180 formations at a high rate, displacing and diluting pre-existing formation fluids. This is
181 typically followed by “shut-in” of a well for days to months prior to flowback. The
182 critical fracturing fluid-shale reaction time is hours to days. Under such conditions, the
183 chemistry of the fracturing fluid will dominate in fracture spaces, and formation fluids

184 may be less important. Therefore an assessment of direct shale-fracturing fluid reactions
185 is required.

186 Approximately 1 g of shale that had been pulverized to between 150 and 250 μm
187 diameter was used in each reactor, with 200 mL of solution and ~ 85 mL of gas-filled
188 headspace with the composition of the laboratory atmosphere. Although the reactors were
189 sealed, limited replenishment of O_2 throughout the experimental duration was facilitated
190 through semi-permeable butyl rubber septa and periodic penetration of the septa with a
191 needle during sampling. A control experiment that lacked shale was conducted for each
192 experimental run time. All reactors contained an $\alpha\text{-Al}_2\text{O}_3$ chip (< 0.05 g) that was meant
193 to serve as a substrate to facilitate precipitation of secondary phases. However, this
194 substrate was found to be ineffective for this purpose. Fluid samples were taken
195 periodically to track pH and cation and anion concentrations. Concentrations of Mg, Ca,
196 Fe, and Si, were measured using inductively coupled plasma optical emission
197 spectroscopy (ICP-OES). Concentrations of Al, Pb, U, Sr, and Ni were measured using
198 inductively coupled plasma mass spectrometry (ICP-MS), and sulfate concentration was
199 measured using ion chromatography (IC). Solids were collected post-reaction and were
200 stored under vacuum in a desiccator prior to analysis with XRD, and scanning electron
201 microscopy (SEM) coupled with energy-dispersive spectroscopy (EDS). Measurements
202 of iron speciation in fluids and solids in our experiments are beyond the scope of the
203 present study, and are instead presented in detail by Jew et al. (*in press*).

204 2.2. Speciation calculations

205 To evaluate the stability of mineral phases in the presence of the fracturing fluid,
206 and the potential for secondary phase formation, speciation calculations were conducted

207 using experimental pH and cation and sulfate concentration data and the geochemical
208 modeling software, PHREEQC V.3 (Parkhurst and Appelo, 2013) with the Lawrence
209 Livermore National Laboratory (LLNL) database. Owing to the dearth of available
210 thermodynamic data to represent the fracture fluid additives, only the additive HCl was
211 included in the models; the organic additives were neglected. Speciation calculations may
212 therefore overestimate the saturation state of mineral phases if significant complexation
213 of inorganic ions with fracture additives or organic complexes native to the shale samples
214 occurred. It should also be noted that speciation calculations assumed equilibrium
215 between aqueous Fe(II) and Fe(III), despite potential kinetic limitations to aqueous Fe(II)
216 oxidation at low pH (Morgan and Lahav, 2007). Due to a lack of dissolved inorganic
217 carbon (DIC) data, DIC concentrations were assumed to reflect primarily carbonate
218 dissolution and were therefore set to balance dissolved Ca concentrations assuming
219 stoichiometric calcite dissolution, as calcite was determined to be the main source of Ca
220 and the most reactive carbonate phase in the samples (refer to section 3.2.3).

221

222 **3. Results and Discussion**

223 Predictions about the effects of the reaction of hydraulic fracturing fluid with
224 shale on contaminant release, fracturing fluid transport, and hydrocarbon recovery
225 requires identification of the types of reactions that will occur as well as their kinetics.
226 However, the complex mineralogy of shales, the commonality of elements between
227 minerals, and the possibility of incongruent dissolution and secondary mineral
228 precipitation confound the direct attribution of aqueous solute concentrations to specific
229 mineral dissolution-precipitation reactions. To address this, we use multiple lines of

230 evidence to determine the mineral dissolution-precipitation reactions that are most likely
231 to occur over the typical timescale of hydraulic fracturing operations (weeks to months)
232 as well as the shale components that govern the evolution of fluid composition and rock
233 porosity and permeability.

234 *3.1 Evolution of fluid composition*

235 *3.1.1. Calcium, magnesium, and pH*

236 Of the major elements initially present in the shales, Ca was released into the
237 fracturing fluid to the greatest extent. In all experiments the release of Ca was initially
238 rapid, before plateauing at reasonably stable values within 48 h (Figure 1a). The steady-
239 state Ca concentrations differed among the four shales and did not correspond directly to
240 the Ca content of the solid phases. The highest aqueous Ca concentration was recorded
241 for the EF shale, followed by the M, the GR, and finally, the B shales (Figure 1a). Yet,
242 the initial solid Ca content of the GR shale exceeded that of the M shale (Table 1). The
243 maximum aqueous Ca values during three weeks of reaction were EF (318 mg L⁻¹), M
244 (242 mg L⁻¹), GR (221 mg L⁻¹), and B (192 mg L⁻¹) (Figure 1a). Aqueous Ca
245 concentrations remained relatively stable in both the intermediate- and long-term
246 experiments (Figure 2a), indicating that the majority of Ca release occurred within 48 h.
247 Different Ca concentrations (up to ~30% different) were observed between duplicate M
248 reactors in both the intermediate- and long-term experiments, which is attributed to
249 mineralogical heterogeneity of the starting solids (Figure 2a). Small differences in Ca
250 concentration trends between the short-term Barnett duplicates are also attributed to
251 heterogeneity of the initial solids. The Marcellus exhibited a large degree of
252 heterogeneity visible at the millimeter scale (SI Figure S2). The smaller degree of

253 heterogeneity in the Barnett samples compared to the Marcellus samples is attributed to
254 different sampling protocols; the Barnett was sampled from core, whereas the Marcellus
255 was sampled from outcrop.

256 Trends in Mg release to solution were similar to those observed for Ca for the GR, M,
257 and B shales, with a rapid initial increase within 48 h, followed by relatively stable
258 concentrations for the remainder of the short-term experiments (SI Figure S3). However,
259 maximum aqueous Mg concentrations were lower than Ca solution concentrations, with
260 less than 50 mg L⁻¹ Mg for all four shales. This is consistent with the lower solid phase
261 Mg content for all shales (Table 1). Similar to Ca, Mg concentrations remained relatively
262 stable for the durations of the intermediate- and long-term experiments for the GR, M,
263 and B shales, suggesting that the majority of Mg release also occurred within the first 48
264 h of reaction (SI Figure S3). Although Mg content in the initial shale material for EF was
265 similar to B and M (Table 1), the total concentration of Mg in solution was significantly
266 lower (< 3 mg L⁻¹) in the short- and intermediate-term experiments, and remained below
267 quantifiable limits for the long-term experiment (*i.e.*, <1 mg L⁻¹).

268 In all experiments the rapid increases in Ca concentrations within 48 h coincided with
269 rapid increases in solution pH (Figure 1a,b). In fact, two distinct trends in fluid pH were
270 evident in the experiments as a function of the initial carbonate mineral content of the
271 rock. The carbonate-rich EF and GR shales exhibited rapid pH increases from values of
272 ~2 before plateauing at circum-neutral values within 48 h, which coincided with plateaus
273 in Ca concentration (Figure 1b). The pH was maintained at circum-neutral levels
274 throughout the durations of the intermediate- and long-term carbonate-rich shale reactors
275 (Figure 2b). Conversely, the pH for the carbonate-poor B and M reactors remained acidic,

276 plateauing at values between 3 and 5 for experiments of all durations up to six months
277 (Figures 1b and 2b). Differences in fluid pH between duplicate reactors were documented
278 for the intermediate- and long-term M reactors, as was observed for Ca concentrations
279 and was attributed to sample heterogeneity (Figure 2b). The experiments with higher pH
280 corresponded to those with higher Ca concentrations.

281 *3.1.2. Iron release*

282 All Fe concentrations reported represent total aqueous Fe as measured with ICP-OES.
283 Iron concentrations were too low to be quantified using our analytical techniques for the
284 GR and EF shales in reactors of all timescales ($< \sim 0.3$ ppm). Aqueous Fe concentrations
285 for both the M and B shales, on the other hand, increased rapidly within ~ 200 h. Fe
286 concentrations reached up to 27 mg L^{-1} in the M reactor and 17 mg L^{-1} in the B reactors,
287 after which Fe concentrations declined for both B and M (Figure 1c). However, Fe
288 concentrations did not decline over time in the intermediate- or long-term B reactors.
289 Rather, they oscillated at $\sim 20 \text{ mg L}^{-1}$ for the majority of the intermediate-term reactor and
290 exhibited a gradual increase to 37 mg L^{-1} in the long-term reactor (Figure 2c). As
291 observed for Ca concentrations, duplicate M shale reactors exhibited different Fe
292 concentrations in both the intermediate- and long-term experiments (Figure 2c). Iron
293 concentrations oscillated between 12 and 32 mg L^{-1} in one intermediate-term experiment,
294 but remained below 14 mg L^{-1} in the duplicate experiment. A more pronounced
295 difference was documented for the long-term experiments; the Fe concentration
296 continued to gradually increase throughout the experimental duration in one reactor,
297 reaching up to 37 mg L^{-1} , whereas the Fe concentration was fairly stable between 3 and 6
298 mg L^{-1} for the duplicate experiment (Figure 2c).

299

300 *3.1.3. Sulfate release*

301 Unlike the decline observed for Fe, aqueous SO_4^{2-} concentrations increased
302 throughout the short-term B and M experiments (Figure 1d). Similarly, in the short-term
303 EF experiment, SO_4^{2-} concentrations increased throughout the experimental duration,
304 despite the lack of measurable Fe in solution. In the GR reactors, on the other hand,
305 aqueous SO_4^{2-} concentrations remained below quantifiable values. This is a consequence
306 of the minimal pyrite in this shale. The differences observed for the concentrations of
307 other elements (Ca, Fe) and pH between duplicate M experiments were less pronounced
308 for SO_4^{2-} . The SO_4^{2-} concentrations were similar between duplicate M intermediate-term
309 reactors, and stabilized after 722 h between 134 and 147 mg L^{-1} . In the long-term
310 experiments, SO_4^{2-} concentrations stabilized within 966 h, plateauing at $\sim 140 \text{ mg L}^{-1}$ in
311 one reactor and $\sim 170 \text{ mg L}^{-1}$ in the other reactor (Figure 2d). A similar extent of sulfate
312 release was observed for the long-term compared to the intermediate-term experiments
313 for all shales, except for the EF, for which a maximum of 98 $\text{mg L}^{-1} \text{SO}_4^{2-}$ was measured
314 in the intermediate-term compared to 141 mg L^{-1} in the long-term experiment (Figure
315 2d).

316 Pyrite was the only S-bearing phase detected with XRD (Table 2), therefore its
317 release to solution is attributed primarily to pyrite dissolution. Mass balance calculated
318 with respect to the XRF-measured sulfur content of the initial solids and final aqueous
319 SO_4^{2-} concentrations revealed that approximately 38%, 37%, 39%, and 36% of the total
320 initial pyrite mass was oxidized within three weeks of reaction in the EF, M, and
321 duplicate B experiments, respectively (SI Figure S4). The extent of pyrite oxidation

322 remained less than 55% in all intermediate- and long-term EF, M, and B experiments,
323 except for the long-term EF experiment, for which up to 72% of pyrite was calculated to
324 have been reacted (SI Figure S4). In all cases, the majority of pyrite oxidation occurred
325 within the first three weeks of exposure to the simulated fracturing fluid. This result
326 implies that the injection of oxic fracturing fluids will induce oxidative dissolution of
327 pyrite, releasing Fe and SO_4^{2-} into produced waters on a timescale of hours to weeks.

328 *3.1.3. Aluminum and silicon*

329 The experiments were conducted in borosilicate reactors and contained Al_2O_3
330 substrates; these could release Si and Al to solution. The extent of dissolution of these
331 components of the reactors was assessed by comparing Si and Al concentrations in the
332 controls that lacked shale to reactors that contained shale. There was negligible Al and Si
333 release in the short-term controls, confirming that changes in Al and Si concentrations in
334 the short-term experiments are attributable to reaction of shale components. However, in
335 the intermediate- and long-term experiments, Al and Si concentrations in most reactors
336 were not substantially different from those measured in the control experiments.
337 Therefore Si and Al cycling occurring in these experiments due to reaction of the shale
338 components alone cannot be assessed, and further discussion is limited to the short-term
339 experiments.

340 There was very little net mass transfer of Al and Si from the solid to fluid phase in the
341 short-term reactors (Figure 3c). The greatest extent of Si release in the short-term reactors
342 was documented for the GR shale, reaching 16 mg L^{-1} , whereas similar concentrations of
343 $<10 \text{ mg L}^{-1}$ were documented for the other three shales (Figure 3a). Al was released to the
344 greatest extent from the Marcellus and Barnett shales, but nevertheless remained below 3

345 mg L⁻¹ in all short-term reactors (Figure 3b). This is consistent with the known slow
346 dissolution rates of the silicate minerals present in these shales (Palandri and Kharaka,
347 2004).

348

349 *3.2 Identification and kinetics of key reactions*

350 *3.2.1 Iron cycling reactions*

351 The presence of multiple Fe-bearing phases of varying, and often poorly-constrained
352 reactivity in shales (Carroll et al., 2013), and the array of secondary Fe-bearing minerals
353 that can form (*e.g.*, goethite [FeO(OH)], hematite [Fe₂O₃], amorphous Fe(OH)₃; Blowes
354 et al., 1998; Nordstrom, 1982), complicates attribution of the sources of dissolved Fe and
355 the prediction of its fate. The potential sources of dissolved Fe in the four shales include
356 Fe-bearing carbonate minerals (siderite or (Mg-Ca-Fe)_xCO₃ solid solutions), clays (illite,
357 smectite, and chlorite-group minerals), organic matter, and pyrite. The low extent of Si
358 and Al release in all experiments is consistent with the relatively slow dissolution rates of
359 aluminosilicate minerals compared to carbonate minerals and pyrite (*i.e.*, 10^{-5.81} mol/m²/s,
360 10^{-4.55} mol/m²/s, 10^{-9.12} mol/m²/s, and 10^{-12.78} mol/m²/s for calcite, pyrite, anorthite, and
361 smectite, respectively, at 25°C and neutral pH; *c.f.*, Palandri and Kharaka, 2004; Golubev
362 et al., 2009; Rimstidt and Vaughan, 2003; Smith et al., 2013), and suggests that the
363 dissolution of clays was not the main contributor of dissolved Fe in the experiments.
364 Rather, the substantial increase in aqueous SO₄²⁻ concentration in all experiments with
365 pyrite-bearing shales (EF, B, and M) indicates that dissolution of pyrite was an important
366 control on Fe release. The GR shale used in the experiments lacked detectable pyrite
367 based on XRD characterization, although minor pyrrhotite [Fe_(1-x)S] was detected with

368 XRF mapping (Jew et al., *in press*), and neither dissolved Fe nor SO_4^{2-} reached
369 quantifiable concentrations in these reactors.

370 Pyrite is interpreted to be the main source of aqueous SO_4^{2-} , therefore deviation of
371 Fe: SO_4^{2-} molar ratios from stoichiometric pyrite values (0.5) are indicative either of
372 secondary phase precipitation, which preferentially removes one element over the other,
373 or dissolution of other Fe-bearing minerals. The Fe concentrations that would be
374 produced from stoichiometric pyrite dissolution based on measured SO_4^{2-} concentrations
375 were calculated for all pyrite-bearing shales (Figures 1c and 2c). Measured Fe
376 concentrations that are less than calculated Fe concentrations are indicative of
377 precipitation of Fe-bearing phases, whereas measured Fe concentrations that are greater
378 than calculated values indicate either precipitation of SO_4^{2-} -bearing phases or an
379 additional source of Fe in the experiments (*e.g.*, siderite dissolution). For M shale, Fe
380 concentrations declined below stoichiometric values after 200 h in the short-term
381 experiments and remained significantly lower ($>8 \text{ mg L}^{-1}$ lower) than stoichiometric
382 throughout the durations of the intermediate- and long-term experiments (Figures 1c and
383 2c). Similarly, Fe concentrations were below detection for the EF experiments, yet
384 stoichiometric pyrite dissolution would generate up to 26, 28, and 48 mg L^{-1} Fe in the
385 short-, intermediate-, and long-term experiments, based on SO_4^{2-} concentrations. The
386 oxidative dissolution of pyrite is commonly accompanied by precipitation of secondary
387 Fe(III)-bearing (hydr)oxide phases (Blowes et al., 1998; Nordstrom, 1982), and
388 speciation calculations revealed that amorphous $\text{Fe}(\text{OH})_3$ became supersaturated in M
389 reactors within 24 h (Figure 4a). Moreover, rust-colored precipitates were observed in
390 suspension and coating the walls of the reactors for both the M and B experiments of all

391 durations, suggesting the presence of oxidized Fe-bearing secondary phases (SI Figure
392 S5). Though the lack of aqueous Fe data for the EF experiments precludes direct
393 calculation of the saturation indices of Fe-bearing minerals, the Fe concentration
394 necessary to saturate the fluid with respect to amorphous Fe(OH)₃ in these experiments is
395 sufficiently low such that the solutions may have been saturated with respect to this phase
396 without measurable Fe concentrations. The removal of iron from solution relative to
397 sulfate in both the M and EF experiments is thus inferred to reflect the precipitation of
398 secondary Fe(III)-(oxy)hydroxide phase(s). Similarly, the observation of rust-colored
399 precipitates coating reacted GR particles indicates that Fe(III)-bearing precipitates were
400 also formed in these experiments (SI Figure S5), despite the lack of pyrite. Pyrrhotite was
401 identified with synchrotron-based XRF mapping at low abundance and as the main host
402 of Fe in these samples before reaction (Jew et al., *in press*), suggesting pyrrhotite rather
403 than pyrite dissolution may have been the source of Fe in the GR experiments. Fe(III)-
404 bearing precipitates were not present in sufficient quantities in any of the experiments to
405 identify with XRD.

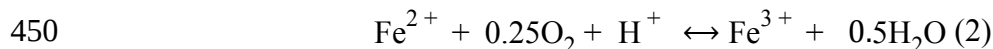
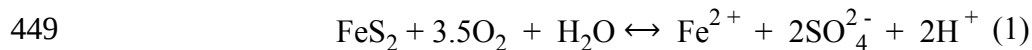
406 In contrast to the M and EF, the B exhibited greater Fe release than can be attributed
407 to stoichiometric pyrite dissolution within the first 100 h of reaction, and in the
408 intermediate- and long-term B experiments, Fe concentrations remained in excess of
409 those predicted by stoichiometric pyrite dissolution for the majority of the experimental
410 durations (Figures 1c and 2c). The rapid increase in Fe concentration relative to sulfate at
411 the beginning of the experiments implies that a mineral with a rapid dissolution rate, such
412 as siderite or Fe-bearing calcite, was also contributing Fe to solution. This implication
413 could also result in excess Fe concentrations compared to stoichiometric pyrite

414 dissolution in the longer-term experiments. Alternatively, precipitation of S-bearing
415 phases could produce the apparent excess in Fe concentration, and would also serve to
416 clog pore spaces. Speciation calculations revealed that Ca-sulfate minerals were not
417 saturated in the bulk solution, yet precipitates containing Ca, S, and O were identified
418 with SEM and EDS in B samples from the long-term experiments (SI Figures S6 and S7).
419 As such, it is not certain whether these precipitates formed *in situ* during the experiments,
420 or were an artifact formed when the samples were dried following the experiment. If
421 formed during the experiments, these precipitates could account for the excess Fe in
422 solution with respect to stoichiometric pyrite dissolution. However, following the initial
423 rapid release, Fe concentrations in the short-term B experiments declined below
424 stoichiometric values for pyrite dissolution after 95 h (Figure 1c), which is again
425 attributed to the formation of Fe(III)-(oxy)hydroxide. Similarly, the lack of measurable
426 aqueous Fe throughout the EF and GR experiments and the decline in Fe concentration
427 after 95 h in the M experiment implies that precipitation of Fe(III)-(oxy)hydroxides
428 began at least within 95 h in these experiments. This conclusion suggests precipitates
429 could form within hours of hydraulic fracturing and could have significant consequences
430 on the transport and recovery of hydrocarbons and the compositions of flowback and
431 produced waters.

432 3.2.2. Controls on pyrite oxidation

433 The dissolution of pyrite from oil and gas shales is of concern, as it is known to
434 release trace metal contaminants, including As, Pb, and Hg (Rimstidt and Vaughan,
435 2003); therefore, it is important to constrain the extent of pyrite reaction that may occur
436 upon injection of oxidized fracturing fluids into shales. In our experiments, the

437 incomplete reaction of pyrite (SI Figure S4) indicates that its dissolution became
438 inhibited over time. There are a number of potential explanations for the apparent
439 inhibition of pyrite dissolution, including: (i) passivation of pyrite surfaces due to
440 precipitation of secondary minerals as surface coatings (Nicholson et al., 1990), (ii)
441 exhaustion of the $O_{2(aq)}$ supply in the reactor, as O_2 is required for oxidative pyrite
442 dissolution, or (iii) pyrite grains located near the surface of the shale particles were
443 consumed at early times, leaving the remaining pyrite within the interior of shale particles
444 poorly exposed to the reactive fluid. This latter possibility is dismissed, as numerous
445 pyrite grains exposed on the surfaces of reacted shale particles were observed with SEM.
446 On the other hand, because the oxidation of pyrite, aqueous Fe(II), and other redox-active
447 components consumes O_2 (Eqs. 1 and 2), the dissolution of pyrite may be self-limiting
448 due to the removal of O_2 as a reactant.



451 Using the initial O_2 content of the reactors as a lower limit to the amount of O_2 available,
452 and assuming the reaction stoichiometry in equations 1 and 2 and no additional O_2 -
453 consuming reactions, mass balance calculations reveal that there was sufficient oxygen
454 present to facilitate further pyrite reaction in all experiments, except perhaps one long-
455 term M reactor (SI Figure S4). Moreover, the semi-permeable nature of the butyl rubber
456 stoppers facilitated some replenishment of O_2 from the laboratory air. Conversely, the
457 precipitation of Fe-(oxy)hydroxides was inferred from fluid compositions (section 3.2.1.).
458 This inference implies that the incomplete reaction of pyrite in the experiments is more

459 likely attributable to passivation of the pyrite surface via precipitation of Fe-
460 (oxy)hydroxide phases as surface coatings than to a lack of O₂.

461 Although the availability of O₂ was not limiting for pyrite reaction in the
462 experiments, this may not be the case at field scale during hydraulic fracturing operations
463 due to the highly reducing conditions of shale reservoirs, and the higher rock to O₂ ratio
464 than used in our experiments. For example, during a typical hydraulic fracturing
465 operation in the Marcellus shale, approximately 1.7×10^4 m³ of oxygenated fracturing
466 fluid may interact with $\sim 1.5 \times 10^7$ m³ of shale (Balashov et al., 2015). Assuming the same
467 pyrite abundance as in the Marcellus experiments and initial equilibrium of the fluid with
468 respect to atmospheric pO₂, these estimates imply a dissolved O₂ to pyrite molar ratio of
469 3.7×10^{-7} , which is far less than that required to completely oxidize the pyrite (*i.e.*, a ratio
470 of 3.5; Eq. 1). Only $1.0 \times 10^{-5}\%$ of the pyrite would be oxidized under this scenario,
471 implying a similarly low percentage of release of trace metals via its dissolution, if
472 dissolution were to occur stoichiometrically. This suggests that at the scale of typical
473 hydraulic fracturing operations, the amount of pyrite oxidation that can occur will be
474 limited by the O₂ supply when the fluid is imbibed into the matrix. If the fluid is not
475 imbibed to a great extent, the reaction may occur mainly at the fracture-matrix interface,
476 where the supply of O₂ could still be excessive. Similarly at grain scale, the precipitation
477 of Fe-(oxy)hydroxides as surface coatings on pyrite may severely limit the reaction rate
478 of individual pyrite grains, effectively stopping pyrite oxidation. In either case, the
479 magnitude of release of contaminants such as Pb from pyrite dissolution will be governed
480 in part by the amount of oxygen injected into the subsurface, which is a function of the
481 concentration of dissolved oxygen in and the volume of the fracturing fluid injected, and

482 the degree to which this fluid is imbibed into the matrix. The rock:fluid ratios are high in
483 the subsurface, thus even the reaction of a small proportion of reactive phases like pyrite
484 at the fracture-fluid interface may strongly alter the fluid composition.

485 3.2.3. *Dissolution of carbonate minerals*

486 There are a number of minerals in all of the shales that could dissolve to release Ca
487 and Mg to solution, including the carbonate minerals calcite [CaCO₃] and dolomite
488 [Ca,Mg(CO₃)₂], illite, smectite, and chlorite-group clay minerals, and plagioclase feldspar
489 (Ca-endmember anorthite [CaAl₂Si₂O₈]). Dissolution of carbonate minerals is rapid
490 compared to dissolution of aluminosilicate minerals, and calcite dissolution in particular
491 is rapid compared to dolomite dissolution (Palandri and Kharaka, 2004; Pokrovsky et al.,
492 2005). The relatively low degree of Si and Al release in these experiments compared to
493 Ca is consistent with the large differences in dissolution rates of Ca-bearing minerals, and
494 implies that aluminosilicates were not the primary source of dissolved Ca in these
495 experiments. Dissolution of carbonate minerals, on the other hand, is rapid and provides
496 alkalinity to solution. Thus, the coincidence of rapid Ca release rates and rapid pH
497 increases are consistent with Ca-carbonate mineral dissolution as the main source of
498 dissolved Ca in these experiments. Analysis of the shales following reaction with XRD
499 confirmed a reduction of calcite content in all shales, whereas the abundances of dolomite
500 and clays were less altered (Jew et al., *in press*). We conclude that calcite dissolution was
501 the primary source of dissolved Ca for both carbonate-poor and carbonate-rich shales.
502 However, the occurrence of plateaus in Ca concentration and the magnitude of Ca
503 concentration at these plateaus are attributed to different factors for the carbonate-rich
504 compared to the carbonate-poor shales.

505 Speciation calculations revealed that coincident Ca concentration and circum-neutral
506 pH plateaus for the carbonate-rich shales (EF and GR) are associated with achievement of
507 equilibrium with respect to calcite (Figure 5); the fluid reached saturation with respect to
508 calcite within 48 h and remained approximately at equilibrium throughout the remainder
509 of the short-term experiments. Similarly, throughout the intermediate- and long-term EF
510 and GR experiments, fluids remained approximately at equilibrium with respect to
511 calcite. In contrast, for the carbonate-poor B and M shales, the solutions remained
512 undersaturated with respect to calcite for experiments of all durations (Figure 5). Mass
513 balance calculations based on bulk XRF analysis of the initial materials and final aqueous
514 Ca concentrations revealed that these carbonate-poor shales were almost completely
515 stripped of Ca within three weeks, whereas the carbonate-rich EF and GR shales
516 maintained more than 70% of their initial Ca over the same time period (inset Figure 1a).
517 The plateaus in Ca concentration and pH are attributed to the exhaustion of the accessible
518 calcite for the carbonate-poor shales, and to the achievement of equilibrium with respect
519 to calcite for the carbonate-rich shales. The magnitude of the Ca concentration at these
520 plateaus is therefore dictated by the mass of fluid-accessible calcite for the carbonate-
521 poor shales, and the extent of dissolution required to achieve equilibrium for the
522 carbonate-rich shales. The concentration of Ca and fluid pH at equilibrium with respect to
523 calcite will differ slightly between the experiments and field conditions due to the lower
524 pressure used in the experiments.

525 Calcite dissolution generates alkalinity, yet the oxidative dissolution of pyrite
526 generates acidity. Both reactions were documented to occur on a similar timescale in all
527 experiments with pyrite-bearing shales. The pH of the fluid at which the pH values

528 plateau therefore reflects the balance between the extent of pyrite dissolution and the
529 abundance of calcite available to buffer the fluid pH. In the case of the carbonate-poor
530 shales (B and M), fluids remained acidic as there was insufficient calcite available to
531 counterbalance the combined acidity of the initial fracturing fluid and that generated from
532 pyrite oxidation. Conversely, the carbonate-rich EF and GR shales had sufficient
533 alkalinity-generating capacity to neutralize all acidity. The extent of calcite dissolution
534 that occurs in a shale formation will therefore depend on the initial pH and volume of the
535 injected fluid, as well as the abundance of pyrite in the shale and amount of dissolved
536 oxygen in the injected fluids.

537 Notably, dolomite, another fairly abundant carbonate mineral in these shales (Table
538 2), remained undersaturated in the B and M experiments, was close to equilibrium in the
539 short- and intermediate-term EF experiments, and was slightly supersaturated in the GR
540 experiments (SI Figure S8). The saturation state of siderite [FeCO₃] could not be
541 calculated for the EF and GR experiments due to the lack of aqueous Fe concentration
542 data, but it remained undersaturated in the B and M experiments. This finding implies
543 that although dissolution of these other carbonate minerals likely occurred, calcite exerted
544 the strongest control on overall fluid pH and Ca concentrations. The low Mg
545 concentrations documented in the EF shale experiments indicate little dolomite
546 dissolution occurred, despite the solutions approaching equilibrium with respect to
547 dolomite. The similar temporal trends in aqueous Mg compared to Ca indicate it was
548 likely sourced from the dissolution of Mg-bearing calcite for the B and M shales.

549

550

551 *3.3 Alteration of porosity*

552 *3.3.1. Porosity generation*

553 Discrete holes of size similar to intact calcite grains in unreacted material (10s of
554 microns) were observed post-reaction in the B shale for all experimental durations
555 (Figure 6). These holes are attributed to the preferential dissolution of calcite. The
556 generation of large, isolated pores was not observed for the M shale, despite the removal
557 of the majority of the calcite from this shale (Figure 6). This result is attributed to
558 differences in initial calcite distribution and size between the two carbonate-poor shales;
559 the calcite in the M was distributed as clusters of smaller grains (<10 μm), compared to
560 generally larger (~15-50 μm), isolated grains in the B (SI Figures S9 and S10). In the EF
561 shale, calcite was also generally distributed as large, isolated grains (SI Figure S11).
562 Changes in surface morphology of the EF were not broadly evident, but some particles
563 did exhibit a mottled texture indicative of porosity generation (Figure 6).

564 Unlike the other shales, calcite was distributed as pervasive cement that filled the
565 areas between silicate and dolomite grains in the GR shale (SI Figure S12). The
566 preferential dissolution of this calcite cement generated a mottled, spongy texture over
567 the majority of the GR shale surface, consistent with the generation of a porosity network
568 (Figure 6). We inferred from aqueous compositions that ~30% of the calcite was lost
569 from the GR shale. Assuming uniform reaction, this translates to a reaction front
570 penetrating ~42 μm deep in each GR particle, and approximately a 1.5-fold increase in
571 the total estimated bulk pore volume of the particles (initial porosity estimated at 10%;
572 Law et al., 1986). Although the secondary porosity network did not appear to be as
573 uniform in the other shales, the calculated bulk pore volume increase for the entire shale

574 mass of each type was similar. The increase in bulk pore volume was estimated to be 3.0-
575 , 2.2-, and 3.4-fold for the B, EF, and M shales, respectively, based on mass balance
576 estimates of calcite loss, and initial porosity values of 3%, 9%, and 4%, respectively
577 (Chalmers et al., 2012; Jennings and Antia, 2013; Law et al., 1986).

578 Our experiments reveal that the interaction of the calcite-bearing shales with acidic
579 fracturing fluid will generate porosity due to calcite dissolution, but the connectivity and
580 distribution of this porosity is dictated by the pore-scale distribution of calcite. Isolated
581 calcite grains tended to generate discrete pores, whereas more homogeneous calcite
582 distribution appeared to result in a more pervasive secondary porosity network. It is well
583 known that even minor changes in porosity can profoundly influence the permeability of
584 a rock (Andreani et al., 2009; Gouze and Luquot, 2011; Luquot et al., 2012; Luquot and
585 Gouze, 2009; Smith et al., 2013), but the net effect of the generated porosity on fluid
586 transport in these shales requires further investigation. It is possible that secondary
587 porosity could enhance the transport of hydrocarbons across the matrix-fracture interface
588 by increasing permeability. Alternatively, hydrocarbon and fluid transport could be
589 inhibited due to capillary effects or weakening of the shale matrix and the subsequent
590 collapse of fractures and large pores. The higher pressure in shale formations compared
591 to our experiments is likely to exert a strong control on the importance of these porosity-
592 altering reactions on permeability, and the imbibition of the fluid into the matrix, which
593 requires further investigation. The manner in which permeability evolves under stress is
594 impacted by shale mineralogy; clay-rich shales tend to exhibit greater pore-throat
595 compressibility (Al Ismail and Zoback, 2016). Therefore the observed geochemical
596 reactions may alter the response of shale permeability to the stresses experienced during

597 hydraulic fracturing due to changes in composition and distribution of pore types and
598 sizes. Regardless, our experiments reveal that geochemical reactions have the potential to
599 alter porosity, and the manner in which it is altered will depend not only on the
600 abundance, but also on the distribution of highly reactive phases such as calcite.

601

602 *3.3.2. Porosity occlusion*

603 *3.3.2.1 Fe(III)-bearing precipitates*

604 Pyrite is the main source of aqueous Fe and SO_4^{2-} from the M and EF shales, thus
605 the deficit between measured Fe concentrations and those expected for stoichiometric
606 pyrite dissolution can be used to approximate the volume of Fe-(oxy)hydroxide
607 precipitated. In the B experiments, an additional source of Fe precludes simple mass
608 balance calculation. In the case of the M and EF, the main reaction product is inferred to
609 be amorphous $\text{Fe}(\text{OH})_3$ in the short-term experiments. Assuming a density of ferrihydrite
610 (3.96 g/cm^3 ; Jambor and Dutrizac, 1998), the volume of $\text{Fe}(\text{OH})_3$ precipitated is only
611 ~4% and 6% of the pore volume generated via calcite dissolution for the EF and M
612 shales, respectively. Despite the reddish coloration observed in the reactors, Fe-
613 (oxy)hydroxides were not observed with SEM, which is consistent with the calculated
614 low volume of precipitates. Thus, calcite dissolution appears to have more strongly
615 influenced the evolution of porosity than did precipitation of secondary phases.
616 Nevertheless, depending on the location in which precipitates form, for example in pore
617 throats versus large pores, they may exert an important control on the transport properties
618 of the rock even with a small volume precipitated (Andreani et al., 2009; Gouze and
619 Luquot, 2011; Luquot et al., 2012; Luquot and Gouze, 2009; Smith et al., 2013). The

620 formation of Fe(III)-precipitates requires the oxidation of both pyrite and aqueous Fe(II),
621 and therefore the total volume of precipitates that can form will be limited by the amount
622 of oxidizing agents that are injected, particularly dissolved O₂.

623 Although the majority of pyrite oxidation concluded within three weeks, speciation
624 calculations revealed that the type of Fe(III)-bearing precipitate may have changed over
625 time during the intermediate- and long-term experiments, as is consistent with known
626 stability of Fe(III)-(oxy)hydroxides (Cudennec and Lecerf, 2006; Schwertmann et al.,
627 1999). The morphology, size, and density of the precipitates are expected to evolve
628 during these phase transformations (Johnston and Lewis, 1983; Michel et al., 2010),
629 therefore porosity and permeability may have continued to evolve due to these
630 transformations. The crystalline phases hematite and goethite were highly supersaturated
631 during the early stages of the reaction for both the M and B shales, whereas the saturation
632 index of amorphous Fe(OH)₃ declined towards equilibrium in the short-term experiments.
633 However, in the intermediate- and long-term B experiments, the fluids were
634 undersaturated with respect to amorphous Fe(OH)₃, yet close to equilibrium with respect
635 to hematite and goethite (Figure 4). The same was true for duplicate intermediate-term
636 and one of the long-term M experiments. The other long-term M reactor remained close
637 to equilibrium with respect to amorphous Fe(OH)₃ due to the higher pH of this reactor
638 compared to its duplicate (data not plotted). The transition from saturation with respect to
639 amorphous Fe(OH)₃ to the more crystalline Fe(III)-bearing phases suggests that the
640 poorly crystalline precursors may have been replaced by more stable phases over time
641 (Steeffel and Van Cappellen, 1990). Although saturation indices may have been
642 overestimated due to relatively slow aqueous Fe(II) oxidation rates (*i.e.*, not equilibrium),

643 and complexation with organics in the fracture fluid or native to the shale that were not
644 accounted for in the speciation calculations, phase transitions are nevertheless expected in
645 the Fe(III)-(oxy)hydroxide system (Cudennec and Lecerf, 2006; Schwertmann et al.,
646 1999). The reduction in porosity of a reaction layer during similar phase transformations
647 between hydrated Mg-carbonate minerals has been postulated to severely limit reaction
648 rates of dissolving minerals (Harrison et al., 2016, 2015). Though not directly observed in
649 the present study, it is possible that the ripening of secondary phases in the shale-
650 hydraulic fracturing fluid system results in continued porosity and permeability evolution
651 over the longer term even after cessation of pyrite oxidation.

652 *3.3.2.2. Al-bearing precipitates*

653 Colorless, gelatinous suspended solids were observed within 6 h in all of our short-
654 term experiments, including controls, and persisted throughout the intermediate- and
655 long-term experiments. These solids were not successfully recovered from the short-term
656 experiments but were selectively removed at the conclusion of the intermediate- and
657 long-term experiments. Precipitates associated with this gelatinous substance consistently
658 appeared as bulbous, pseudo-spherical entities as observed using SEM (SI Figure S6).
659 EDS analysis indicated that these precipitates are composed of Al, O, and in some cases,
660 Cl, suggesting that they are a poorly-crystalline Al-hydr(oxide) phase (SI Figure S6).
661 Speciation calculations revealed that the Al-hydroxide phases gibbsite [Al(OH)₃] and
662 boehmite [γ -AlO(OH)] became supersaturated within 100 h in all short-term experiments
663 (SI Figure S13). The relatively constant level of supersaturation achieved with respect to
664 these phases in the short-term experiments suggests the aqueous Al concentrations were
665 controlled by precipitation of an amorphous Al-hydr(oxide) phase, which is consistent

666 with the observation of amorphous Al-hydroxide floccs that form during mixing of acidic
667 mine drainage waters with neutral surface waters (Furrer et al., 2002). The presence of
668 these Al-bearing precipitates in the short-term experiments could account for the
669 measured solution compositions, though their presence could not be confirmed with
670 SEM. Like the Fe(III)-(oxy)hydroxides, these Al-hydr(oxides) provide the potential to
671 clog pore space and fracture apertures, as well as acting as surfaces for adsorption of
672 trace metals, should they form in the subsurface. However, both boehmite and gibbsite
673 were undersaturated in the long-term experiments for all shales, suggesting that they may
674 not be stable for long durations.

675

676 *3.4 Contaminant and trace element release*

677 *3.4.1 Lead, uranium, and nickel*

678 One of the major environmental concerns of hydraulic fracturing operations is the
679 potential to contaminate ground or surface waters with toxic or radioactive metals such as
680 As, Pb, and U initially present in the host rock reservoir (Chermak and Schreiber, 2014;
681 Phan et al., 2015; Vengosh et al., 2014). Such contaminants can be released along with
682 other trace elements during dissolution of shale minerals and degradation of organic
683 matter (Jin et al., 2013; Jung et al., 2013; Phan et al., 2015; Tuttle et al., 2009; Wang et
684 al., 2015). To assess the source and fate of contaminant metals in our shale-fracturing
685 fluid experiments, the concentrations of U, Pb, and Ni were tracked with time. Lead is a
686 common trace element in pyrite that can be released upon its dissolution (Rimstidt and
687 Vaughan, 2003), whereas U in the Marcellus shale is primarily hosted in silicate
688 minerals, with up to 20% hosted in carbonate minerals (Phan et al., 2015). Aqueous

689 concentrations of both Pb and U remained too low for accurate measurement for all but
690 the M shale. Nickel is a common minor element in pyrite (Rimstidt and Vaughan, 2003)
691 that was present at higher abundance than U and Pb in the shales we examined (Table 1).
692 Nickel concentrations were therefore tracked to provide insight as to the behavior of the
693 typical pyrite-bound contaminants that were not successfully measured for the EF and B
694 shales.

695 Nickel release from the M and B shales exhibited behavior similar to that of SO_4^{2-} in
696 the short-term experiments, and there was negligible Ni release from the GR shale. These
697 trends are consistent with Ni being sourced primarily from pyrite dissolution (Figure
698 7a,b). Declines in Ni concentration were observed in the intermediate- and long-term EF
699 experiments, and remained relatively stable throughout the durations of the intermediate-
700 and long-term B experiments (Figure 7a). Nickel concentrations also exhibited moderate
701 declines in the intermediate- and long-term M experiments, and the maximum
702 concentrations differed between duplicate reactors, as was documented for Ca, Fe, and
703 pH (Figure 7b).

704 Similar to Ni, the temporal trend in aqueous Pb concentration mimicked that of SO_4^{2-}
705 in the short-term M experiments, implying that Pb was also released from dissolving
706 pyrite (Figure 7c). Conversely, U was released rapidly from the M shale in the first 24 h,
707 after which its concentration continued to increase at a much slower rate, reaching a
708 maximum of $64 \mu\text{g L}^{-1}$ in the short-term experiments (Figure 7d). This result for U is
709 similar to the behavior of Ca and fluid pH, implying that U is primarily sourced from
710 carbonate dissolution, which is consistent with observations of Phan et al. (2015).
711 However, both U and Pb concentrations exhibited pronounced declines over time in one

712 each of the duplicate intermediate- and long-term M experiments (Figures 7c,d). In the
713 other duplicate reactors, U, and Pb concentrations remained significantly lower
714 throughout the experimental durations (Figure 7d). The reactors with low aqueous
715 concentrations of U, Pb, and Ni were also those for which aqueous Ca concentrations and
716 pH were high, but Fe concentrations were low. A comparison of maximum U, Pb, and Ni
717 concentrations versus maximum fluid pH for the M reactors of all durations reveals a
718 tendency of lower U, Pb, and Ni concentration with higher pH (Figure 8a). Sulfate release
719 occurred to a similar magnitude in both intermediate-term M duplicates, and sulfate
720 concentrations were higher in the long-term duplicate experiment with lower Ni, U, and
721 Pb concentrations, indicating that the lower aqueous concentrations of these trace
722 elements cannot be attributed to less pyrite dissolution. Rather, like the concentrations of
723 these trace elements, a tendency toward lower aqueous Fe:S molar ratio as a function of
724 pH was observed in the M reactors (Figure 8b), which is indicative of a greater extent of
725 Fe-(oxy)hydroxide precipitation in the reactors with higher pH. The removal of U, Pb,
726 and Ni from solution likely reflects adsorption at the surface of and/or co-precipitation
727 with these secondary (oxy)hydroxide phases, a well-known phenomenon (Bargar et al.,
728 1997; Benjamin and Leckie, 1981; Bruno et al., 1995; Duff et al., 2002; Enid Martinez
729 and McBride, 1998). This greater degree of Fe-(oxy)hydroxide precipitation is facilitated
730 by a faster rate of aqueous Fe(II) oxidation, which increases as a function of pH (Morgan
731 and Lahav, 2007; Stumm and Lee, 1961), and resulted in lower aqueous concentrations of
732 trace metals for the M reactors. A similar process could account for the decline in Ni
733 concentrations in the EF reactors, implying that trace metal contaminants may also be
734 removed in this fashion for the EF shale. The stabilization of Ni concentrations in the

735 longer-term experiments for the B and GR shales may indicate the cessation of
736 dissolution of the source phase for Ni; therefore, it is not clear whether sequestration of
737 trace metals was occurring in these experiments.

738 Although the formation of precipitates may serve to clog porosity and inhibit
739 hydrocarbon recovery, they may also be beneficial due to the apparent mitigation of
740 contaminant release. However, the transformation from less to more stable phases over
741 time may affect the sorption capacity of the secondary phases, therefore contaminant
742 concentrations may continue to evolve along with porosity. As both the precipitation of
743 (oxy)hydroxides and the subsequent sorption of metals are favored at higher pH,
744 contaminant mobility will be highly sensitive to the relative proportion of acid and
745 alkalinity-generating reactants – namely the abundance of calcite and pyrite in the shale,
746 and the concentration of dissolved O₂ and acidic additives present in the fracturing fluid.
747 Higher acid concentrations and lower carbonate mineral content will tend to favor
748 mobility of contaminants. These results imply that the contamination of flowback and
749 produced waters will depend not only on the abundance of contaminants in a given shale
750 formation, but on the relative abundance of acidity- and alkalinity-generating minerals.
751 The composition of hydraulic fracturing fluid should be tailored according to shale
752 mineralogy. For example, a more acidic fluid could be used with carbonate-rich shales
753 while still permitting high pH conditions in the formation.

754 3.4.2. *Strontium release*

755 Trace metals such as Sr, which is commonly substituted in carbonate minerals
756 (Tesoriero and Pankow, 1996), can be used as tracers of fluid-rock interaction that help
757 identify sources of flowback and produced waters (Capo et al., 2014; Chapman et al.,

758 2012; Phan et al., 2016). Strontium concentrations were tracked over time in the
759 experiments to assess the degree to which mineral dissolution may control Sr
760 concentrations and isotopic compositions in the subsurface. Strontium exhibited an
761 initially rapid release for all shales in the short-term experiments and plateaued at
762 relatively constant values for the majority of the intermediate- and long-term
763 experiments, comparable to the behavior observed for Ca and Mg (Figure 9). The release
764 of Sr is primarily attributed to the dissolution of carbonate minerals, particularly calcite,
765 as has been observed during reaction of the Gothic shale with brine and CO₂, and was
766 inferred to occur during hydraulic fracturing fluid interaction with Marcellus shale at
767 field scale (Jung et al., 2013; Stewart et al., 2015). Similar to the release of U and Pb, the
768 extent of release of Sr under field conditions will therefore depend primarily on the
769 balance between acidity- and alkalinity-generating reactions and the ensuing extent of
770 carbonate mineral dissolution. The rapid dissolution rate of calcite upon contact with the
771 fracturing fluid highlights that the release of Sr from carbonate minerals in the shale
772 formations must be considered when Sr isotopic compositions of produced waters are
773 used to determine the sources and flow paths of these waters. If the Sr isotopic
774 composition of the carbonate in the shale formation is known, the Sr isotopic composition
775 of the fluid can also be used to help constrain the extent of fluid-rock interaction incurred
776 in the fractured formation.

777

778 **4. Summary and implications for hydraulic fracturing operations**

779 Our experiments revealed that exposure of shales to hydraulic fracturing fluid can
780 induce an array of reactions independent of the exact composition of the shale. The

781 mineralogy of the shale, along with the distribution of the minerals, will strongly dictate
782 the evolution of fluid composition. The simulated fracturing fluid in our experiments
783 prompted extensive dissolution of calcite and pyrite, and minor dissolution of silicate
784 minerals in all shales containing these minerals. The dissolution of calcite tended to
785 generate porosity, which could serve either to enhance hydrocarbon transport, or may
786 lead to weakening of the shale matrix and collapse of fractures. On the other hand, the
787 formation of secondary (oxy)hydroxide phases will clog pore spaces and may block
788 fracture apertures, a process that may contribute to the field-observed inefficient recovery
789 of hydrocarbons. Mineral dissolution reactions released trace metal contaminants to
790 solution that could be brought to the surface with produced and flowback waters,
791 incurring the risk of contaminating surface waters and necessitating treatment of
792 produced waters for safe disposal or re-use (Vengosh et al., 2013, 2014). However, the
793 precipitates were inferred to remove the contaminants from solution via adsorption and/or
794 co-precipitation, which could partially mitigate contaminant transport in the subsurface.

795 Mineral dissolution-precipitation reactions, rates of aqueous Fe(II) oxidation, and
796 sorption of contaminants are highly sensitive to fluid pH, which was found to be
797 governed most strongly by the mineralogical composition of the rock. Carbonate-rich
798 shales rapidly recovered fluid pH to circum-neutral conditions, whereas fluids in contact
799 with carbonate-poor shales remained acidic. More extensive calcite dissolution generated
800 higher pH, and permitted an apparently greater extent of Fe-(oxy)hydroxide precipitation
801 and more efficient removal of metal contaminants from solution. The implication is that
802 both reaction-induced porosity alteration and the release of contaminants will depend
803 strongly on the volume of fluid injected, as well as the acidity of the fluid and the

804 dissolved oxygen content. Moreover, the mineralogical composition and pore-scale
805 distribution of highly reactive phases, such as pyrite and calcite, will dictate the degree to
806 which contaminants are released and the manner in which porosity develops, as will the
807 effective rock volume with which the fluid reacts (*i.e.*, the degree of imbibition). Further
808 investigation is required to better understand the physical controls on fluid uptake into the
809 matrix and thus the extent of reaction that may occur. In any case, our experiments reveal
810 that both the release of contaminants and formation of porosity-clogging precipitates
811 could be minimized by utilizing fracturing fluids with lower dissolved oxygen content.
812 Although fracturing fluids often include complexing agents designed to inhibit
813 precipitation of secondary phases to minimize mineral scale formation, our experimental
814 results suggest that this practice may counteract the beneficial removal of metal
815 contaminants from solution in the presence of O₂. Overall, our experiments illustrate that
816 fracture fluid compositions and residence times should be adjusted according to shale
817 mineralogy. In carbonate-rich reservoirs, more rapid flushing of fluids, higher acid
818 concentrations, or higher concentrations of Fe-complexing agents would be required
819 compared to carbonate-poor reservoirs to reduce mineral precipitation. In carbonate-poor
820 reservoirs, on the other hand, the low fluid pH may facilitate greater release of metal
821 contaminants (*e.g.*, U, Pb), and therefore more treatment and monitoring of flowback and
822 produced waters may be required. It should also be noted that formation waters typically
823 contain much higher total dissolved solids than were used in our experiments. This
824 difference in initial fluid chemistry may impact some of the reactions observed in our
825 experiments, such as the saturation state of secondary minerals, and the sorption behavior
826 of trace metals. The impacts of high total dissolved solids therefore require further

827 investigation, although the degree to which these fluids may be displaced and diluted, and
828 therefore continue to react within the fractured zone is unknown. Our experiments
829 confirm that a number of reactions can be induced between shales and fluids containing
830 the typical fracturing fluid additives, highlighting the need to better understand these
831 interactions over a variety of geochemical conditions.

832

833 **Supporting Information**

834 A detailed description of the experimental design, analytical methods, speciation
835 calculation results, and supplementary data are available in the Supporting Information.

836

837 **Acknowledgments**

838 This research was funded by a National Energy and Technology Laboratory
839 (NETL), Strategic Center for Natural Gas and Oil, grant to SLAC under Department of
840 Energy Contract DE-AC02-76SF00515. ALH was also partially supported by a
841 postdoctoral fellowship from the Natural Sciences and Engineering Research Council of
842 Canada. We appreciate the analytical assistance of Guangchao Li, Doug Turner, Juliet
843 Jamtgaard, Richard Chin, Bob Jones, and Matt Coble. We would like to thank Arjun
844 Kholi for supplying the core samples of both the Eagle Ford and Barnett shales used in
845 this work. A portion of this work was conducted at the Stanford Nano Shared Facilities at
846 Stanford University. This study benefited greatly from discussion with Andrew Kiss,
847 Arjun Kohli, Cindy Ross, Mark Zoback, Yijin Liu, Anthony Kavscek, Mark Hartney, and
848 David Cercone. We thank two anonymous reviewers whose comments greatly improved
849 this manuscript.

850 **References**

- 851 Al Ismail, M.I., Zoback, M.D., 2016. Effects of rock mineralogy and pore structure on
852 extremely low stress-dependent matrix permeability of unconventional shale gas and
853 shale oil samples. *Phil. Trans. R. Soc. A.* 374, DOI: 10.1098/rsta.2015.0428.
- 854 Ali, M., Hascakir, B., 2015. Water-Rock Interaction for Eagle Ford, Marcellus, Green
855 River, and Barnett. *SPE East. Reg. Meet.* 1–16.
- 856 Andreani, M., Luquot, L., Gouze, P., Godard, M., Hoisé, E., Gibert, B., 2009.
857 Experimental study of carbon sequestration reactions controlled by the percolation
858 of CO₂-rich brine through peridotites. *Environ. Sci. Technol.* 43, 1226–1231.
- 859 Balaba, R.S., Smart, R.B., 2012. Total arsenic and selenium analysis in Marcellus shale,
860 high-salinity water, and hydrofracture flowback wastewater. *Chemosphere* 89,
861 1437–1442.
- 862 Balashov, V.N., Engelder, T., Gu, X., Fantle, M.S., Brantley, S.L., 2015. A model
863 describing flowback chemistry changes with time after Marcellus Shale hydraulic
864 fracturing. *Am. Assoc. Pet. Geol. Bull.* 99, 143–154.
- 865 Barbot, E., Vidic, N., Gregory, K., Vidic, R., 2013. Spatial and temporal correlation of
866 water quality parameters of produced waters from devonian-age shale following
867 hydraulic fracturing. *Environ. Sci. Technol.* 47, 2562–2569.
- 868 Bargar, J.R., Brown, G.E., Parks, G.A., 1997. Surface complexation of Pb(II) at oxide-
869 water interfaces: II. XAFS and bond-valence determination of mononuclear Pb(II)
870 sorption products and surface functional groups on iron oxides. *Geochim.*
871 *Cosmochim. Acta* 61, 2652–2652.
- 872 Benjamin, M.M., Leckie, J.O., 1981. Multiple-site adsorption of Cd, Cu, and Pb on

873 amorphous iron oxyhydroxides. *J. Colloid Interface Sci.* 79, 209–221.

874 Blauch, M.E., Myers, R.R., Moore, T.R., Lipinski, B.A., Houston, N.A., 2009. Marcellus
875 shale post-frac flowback waters - where is all the salt coming from and what are the
876 implications?, *in*: Society of Petroleum Engineers, Eastern Regional Meeting:
877 Charleston, WV, September 23-25.

878 Blowes, D.W., Jambor, J.L., Hanton-fong, C.J., Lortie, L., Gould, W.D., 1998.
879 Geochemical , mineralogical and microbiological characterization of a sulphide-
880 bearing carbonate-rich gold-mine tailings impoundment, Joutel, Quebec. *Appl.*
881 *Geochem.* 13, 687–705.

882 Brantley, S.L., Yoxheimer, D., Arjmand, S., Grieve, P., Vidic, R., Pollak, J., Llewellyn,
883 G.T., Abad, J., Simon, C., 2014. Water resource impacts during unconventional
884 shale gas development: The Pennsylvania experience. *Int. J. Coal Geol.* 126, 140–
885 156.

886 Bruno, J., De Pablo, J., Duro, L., Figuerola, E., 1995. Experimental study and modeling
887 of the U(VI)-Fe(OH)₃ surface precipitation/coprecipitation equilibria. *Geochim.*
888 *Cosmochim. Acta* 59, 4113–4123.

889 Capo, R.C., Stewart, B.W., Rowan, E.R., Kohl, C.A.K., Wall, A.J., Chapman, E.C.,
890 Hammack, R.W., Schroeder, K.T., 2014. The strontium isotopic evolution of
891 Marcellus formation produced waters, southwestern Pennsylvania. *Int. J. Coal*
892 *Geol.* 126, 57–63.

893 Carroll, S.A., McNab, W.W., Dai, Z., Torres, S.C., 2013. Reactivity of Mount Simon
894 Sandstone and the Eau Claire Shale under CO₂ storage conditions. *Environ. Sci.*
895 *Technol.* 47, 252–261.

896 Chalmers, G.R., Bustin, R.M., Power, I.M., 2012. Characterization of gas shale pore
897 systems by porosimetry, pycnometry, surface area, and field emission scanning
898 electron microscopy/transmission electron microscopy image analyses: Examples
899 from the Barnett, Woodford, Haynesville, Marcellus, and Doig units. *Am. Assoc.*
900 *Pet. Geol. Bull.* 96, 1099–1119.

901 Chapman, E.C., Capo, R.C., Stewart, B.W., Kirby, C.S., Hammack, R.W., 2012.
902 Geochemical and strontium isotope characterization of produced waters from
903 Marcellus shale natural gas extraction. *Environ. Sci. Technol.* 6, 3545–3553.

904 Chermak, J.A., Schreiber, M.E., 2014. Mineralogy and trace element geochemistry of gas
905 shales in the United States: Environmental implications. *Int. J. Coal Geol.* 126, 32–
906 44.

907 Cudennec, Y., Lecerf, A., 2006. The transformation of ferrihydrite into goethite or
908 hematite, revisited. *J. Solid State Chem.* 179, 716–722.

909 Duff, M.C., Coughlin, J.U., Hunter, D.B., 2002. Uranium co-precipitation with iron oxide
910 minerals. *Geochim. Cosmochim. Acta* 66, 3533–3547.

911 Enid Martinez, C., McBride, M.B., 1998. Coprecipitates of Cd, Cu, Pb and Zn in iron
912 oxides: Solid phase transformation and metal solubility after aging and thermal
913 treatment. *Clays Clay Miner.* 46, 537–545.

914 FracFocus Chemical Disclosure Registry, 2016. Ground Water Protection Council;
915 Interstate Oil & Gas Compact Commission; <https://fracfocus.org>

916 Furrer, G., Phillips, B.L., Ulrich, K.-U., Pöthig, R., Casey, W.H., 2002. The origin of
917 aluminum flocs in polluted streams. *Science.* 297, 2245–2247.

918 Golubev, S. V., Benezeth, P., Schott, J., Dandurand, J.L., Castillo, A., 2009. Siderite

919 dissolution kinetics in acidic aqueous solutions from 25 to 100°C and 0 to 50 atm
920 $p\text{CO}_2$. *Chem. Geol.* 260, 295–301.

921 Gouze, P., Luquot, L., 2011. X-ray microtomography characterization of porosity,
922 permeability and reactive surface changes during dissolution. *J. Contam. Hydrol.*
923 120–121, 45–55.

924 Haluszczak, L.O., Rose, A.W., Kump, L.R., 2013. Geochemical evaluation of flowback
925 brine from Marcellus gas wells in Pennsylvania, USA. *Appl. Geochem.* 28, 55–61.

926 Hammack, R.W., Harbert, W., Sharma, S., Stewart, B.W., Capo, R.C., Wall, A.J., Wells,
927 A., Diehl, R., Blaushild, D., Sams, J., Veloski, G., 2014. An evaluation of fracture
928 growth and gas/fluid migration as horizontal Marcellus Shale gas wells are
929 hydraulically fractured in Greene County, Pennsylvania. National Energy
930 Technology Laboratory: Pittsburgh, 2014; p 76.

931 Harrison, A.L., Dipple, G.M., Power, I.M., Mayer, K.U., 2016. The impact of evolving
932 mineral-water-gas interfacial areas on mineral-fluid reaction rates in unsaturated
933 porous media. *Chem. Geol.* 421, 65–80.

934 Harrison, A.L., Dipple, G.M., Power, I.M., Ulrich Mayer, K., 2015. Influence of surface
935 passivation and water content on mineral reactions in unsaturated porous media:
936 Implications for brucite carbonation and CO_2 sequestration. *Geochim. Cosmochim.*
937 *Acta* 148, 477–495.

938 Jambor, J.L., Dutrizac, J.E., 1998. Occurrence and constitution of natural and synthetic
939 ferrihydrite, a widespread iron oxyhydroxide. *Chem. Rev.* 98, 2549–2586.

940 Jennings, D.S., Antia, J., 2013. Petrographic characterization of the Eagle Ford shale,
941 South Texas: Mineralogy, common constituents, and distribution of nanometer-scale

942 pore types. *in*: W. Camp, E. Diaz, and B. Wawak, eds., Electron microscopy of shale
943 hydrocarbon reservoirs: AAPG Memoir 102, p. 101–113.

944 Jew, A.D., Dustin, M.K., Harrison, A.L., Joe-Wong, C.M., Thomas, D.L., Maher, K.M.,
945 Brown, G.E. Jr., Bargar, J.R., *in review*. Impact of organics and carbonates on the
946 oxidation and precipitation of iron during hydraulic fracturing of shale. *Energy &*
947 *Fuels*.

948 Jin, L., Mathur, R., Rother, G., Cole, D., Bazilevskaya, E., Williams, J., Carone, A.,
949 Brantley, S., 2013. Evolution of porosity and geochemistry in Marcellus Formation
950 black shale during weathering. *Chem. Geol.* 356, 50–63.

951 Johnston, J.H., Lewis, D.G., 1983. A detailed study of the transformation of ferrihydrite
952 to hematite in an aqueous medium at 92°C. *Geochim. Cosmochim. Acta* 47, 1823–
953 1831.

954 Jung, H.B., Um, W., Cantrell, K.J., 2013. Effect of oxygen co-injected with carbon
955 dioxide on Gothic shale caprock-CO₂-brine interaction during geologic carbon
956 sequestration. *Chem. Geol.* 354, 1–14.

957 Kerr, R.A., 2010. Natural gas from shale bursts onto the scene. *Science.* 328, 1624–
958 1626.

959 Law, B.E., Pollastro, R.M., Keighin, C.W., 1986. Geologic characterization of low-
960 permeability gas reservoirs in selected wells, greater Green River Basin, Wyoming,
961 Colorado, and Utah, *in*: AAPG Special Volumes: SG 24: Geology of Tight Gas
962 Reservoirs. pp. 253–169.

963 Lester, Y., Ferrer, I., Thurman, E.M., Sitterley, K.A., Korak, J.A., Aiken, G., Linden,
964 K.G., 2015. Characterization of hydraulic fracturing flowback water in Colorado:

965 Implications for water treatment. *Sci. Total Environ.* 512–513, 637–644.

966 Luquot, L., Andreani, M., Gouze, P., Camps, P., 2012. CO₂ percolation experiment
967 through chlorite/zeolite-rich sandstone (Pretty Hill Formation – Otway Basin–
968 Australia). *Chem. Geol.* 294–295, 75–88.

969 Luquot, L., Gouze, P., 2009. Experimental determination of porosity and permeability
970 changes induced by injection of CO₂ into carbonate rocks. *Chem. Geol.* 265, 148–
971 159.

972 Materials Data, Inc., 2002. Jade XRD Pattern Processing Ver. 6.5.

973 Michel, F.M., Barrón, V., Torrent, J., Morales, M.P., Serna, C.J., Boily, J.-F., Liu, Q.,
974 Ambrosini, A., Cismasu, a C., Brown, G.E., 2010. Ordered ferrimagnetic form of
975 ferrihydrite reveals links among structure, composition, and magnetism. *Proc. Natl.*
976 *Acad. Sci. U.S.A.* 107, 2787–2792.

977 Morel, F. M. M., J. G. Hering, 1993. Principles and applications
978 of aquatic chemistry. Wiley-Interscience, New York, 588 pp

979 Morgan, B., Lahav, O., 2007. The effect of pH on the kinetics of spontaneous Fe(II)
980 oxidation by O₂ in aqueous solution - basic principles and a simple heuristic
981 description. *Chemosphere* 68, 2080–2084.

982 Nicholson, R. V., Gillham, R.W., Reardon, E.J., 1990. Pyrite oxidation in carbonate-
983 buffered solution: 2. Rate control by oxide coatings. *Geochim. Cosmochim. Acta* 54,
984 395–402.

985 Nordstrom, D. K., 1982. Aqueous pyrite oxidation and the consequent formation of
986 secondary iron minerals. *Acid sulfate weathering*, 37-56.

987 Orem, W., Tatu, C., Varonka, M., Lerch, H., Bates, A., Engle, M., Crosby, L., McIntosh,

988 J., 2014. Organic substances in produced and formation water from unconventional
989 natural gas extraction in coal and shale. *Int. J. Coal Geol.* 126, 20–31.

990 Palandri J. L. and Kharaka Y. K. (2004) A compilation of rate parameters of water–
991 mineral interaction kinetics for application to geochemical modeling. *US Geol. Sur.*
992 *Open File Rep.* 2004-1068.

993 Parkhurst, D.L., Appelo, C.A.J., 2013. Description of input and examples for PHREEQC
994 Version 3 — A computer program for speciation , batch-reaction , one-dimensional
995 transport, and inverse geochemical calculations, in: *U.S. Geological Survey*
996 *Techniques and Methods*, Book 6, Chap. A43, 497 P. Denver, Colorado, p. 497.

997 Phan, T.T., Capo, R.C., Stewart, B.W., Graney, J.R., Johnson, J.D., Sharma, S., Toro, J.,
998 2015. Trace metal distribution and mobility in drill cuttings and produced waters
999 from Marcellus Shale gas extraction: Uranium, arsenic, barium. *Appl. Geochem.* 60,
1000 89–103.

1001 Phan, T.T., Capo, R.C., Stewart, B.W., Macpherson, G.L., Rowan, E.L., Hammack,
1002 R.W., 2016. Factors controlling Li concentration and isotopic composition in
1003 formation waters and host rocks of Marcellus Shale, Appalachian Basin. *Chem.*
1004 *Geol.* 420, 162–179.

1005 Pokrovsky, O.S., Golubev, S. V., Schott, J., 2005. Dissolution kinetics of calcite,
1006 dolomite and magnesite at 25 °C and 0 to 50 atm pCO₂. *Chem. Geol.* 217, 239–255.

1007 Renock, D., Landis, J.D., Sharma, M., 2016. Reductive weathering of black shale and
1008 release of barium during hydraulic fracturing. *Appl. Geochem.* 65, 73–86.

1009 Rimstidt, D.D., Vaughan, D.J., 2003. Pyrite oxidation: A state-of-the-art assessment of
1010 the reaction mechanism. *Geochim. Cosmochim. Acta* 67, 873–880.

1011 Rowan, E.L., Engle, M.A., Kraemer, T.F., Schroeder, K.T., Hammack, R.W., Doughten,
1012 M.W., 2015. Geochemical and isotopic evolution of water produced from Middle
1013 Devonian Marcellus shale gas wells, Appalachian basin, Pennsylvania. *Am. Assoc.*
1014 *Pet. Geol. Bull.* 99, 181–206.

1015 Roychaudhuri, B., Tsotsis, T.T., Jessen, K., 2013. An experimental investigation of
1016 spontaneous imbibition in gas shales. *J. Pet. Sci. Eng.* 111, 87–97.

1017 Schwertmann, U., Friedl, J., Stanjek, H., 1999. From Fe(III) ions to ferrihydrite and then
1018 to hematite. *J. Colloid Interface Sci.* 209, 215–223.

1019 Shih, J.-S., Saiers, J.E., Anisfeld, S.C., Chu, Z., Muehlenbachs, L.A., Olmstead, S.M.,
1020 2015. Characterization and analysis of liquid waste from Marcellus shale gas
1021 development. *Environ. Sci. Technol.* 49, 9557–9565.

1022 Smith, M.M., Wolery, T.J., Carroll, S.A., 2013. Kinetics of chlorite dissolution at
1023 elevated temperatures and CO₂ conditions. *Chem. Geol.* 347, 1–8.

1024 Steefel, C.I., Van Cappellen, P., 1990. A new kinetic approach to modeling water-rock
1025 interaction: The role of nucleation, precursors, and Ostwald ripening. *Geochim.*
1026 *Cosmochim. Acta* 54, 2657–2677.

1027 Stewart, B.W., Chapman, E.C., Capo, R.C., Johnson, J.D., Graney, J.R., Kirby, C.S.,
1028 Schroeder, K.T., 2015. Origin of brines, salts and carbonate from shales of the
1029 Marcellus Formation: Evidence from geochemical and Sr isotope study of
1030 sequentially extracted fluids. *Appl. Geochem.* 60, 78–88.

1031 Stringfellow, W.T., Domen, J.K., Camarillo, M.K., Sandelin, W.L., Borglin, S., 2014.
1032 Physical, chemical, and biological characteristics of compounds used in hydraulic
1033 fracturing. *J. Hazard. Mater.* 275, 37–54.

1034 Stumm, W., Lee, G.F., 1961. Oxygenation of ferrous iron. *Ind. Eng. Chem.* 53, 143–146.

1035 Tesoriero, A.J., Pankow, J.F., 1996. Solid solution partitioning of Sr²⁺, Ba²⁺, and Cd²⁺ to
1036 calcite. *Science*. 60, 1053–1063.

1037 Tuttle, M.L.W., Breit, G.N., Goldhaber, M.B., 2009. Weathering of the New Albany
1038 Shale, Kentucky: II. Redistribution of minor and trace elements. *Appl. Geochem.* 24,
1039 1565–1578.

1040 U.S Energy Information Administration, 2013. Technically recoverable shale oil and
1041 shale gas resources: An assessment of 137 shale formations in 41 countries outside
1042 the United States. EIA report: Washington, D.C., 2013; p 76.
1043 <http://www.eia.gov/analysis/studies/worldshalegas/pdf/overview.pdf>

1044 Vengosh, A., Jackson, R.B., Warner, N., Darrah, T.H., Kondash, A., 2014. A critical
1045 review of the risks to water resources from shale gas development and hydraulic
1046 fracturing in the United States. *Environ. Sci. Technol.* 16, 8334–8348.

1047 Vengosh, A., Warner, N., Jackson, R., Darrah, T., 2013. The effects of shale gas
1048 exploration and hydraulic fracturing on the quality of water resources in the United
1049 States. *Procedia Earth Planet. Sci.* 7, 863–866.

1050 Vidic, R.D., Brantley, S.L., Vandenbossche, J.M., Yoxtheimer, D., Abad, J.D., 2013.
1051 Impact of shale gas development on regional water quality. *Science*. 340, 1235009-
1052 1–1235009-9.

1053 Wang, L., Fortner, J.D., Giammar, D.E., 2015. Impact of water chemistry on element
1054 mobilization from Eagle Ford shale. *Environ. Eng. Sci.* 32, 310–320.

1055 Ziemkiewicz, P.F., Thomas He, Y., 2015. Evolution of water chemistry during Marcellus
1056 shale gas development: A case study in West Virginia. *Chemosphere* 134, 224–231.

1057 Zolfaghari, A., Dehghanpour, H., Noel, M., Bearinger, D., 2016. Laboratory and field
1058 analysis of flowback water from gas shales. *J. Unconv. Oil Gas Resour.* 14, 113–
1059 127.
1060

1061
1062

Table 1. Initial chemical composition of shale samples^a

Element ^b	Barnett	Marcellus	Green River	Eagle Ford
Na (wt.%)	0.10	< 0.01	0.94	< 0.01
Mg (wt.%)	0.63	0.78	4.41	0.37
Al (wt.%)	7.29	10.50	2.66	5.82
Si (wt.%)	25.53	28.41	12.27	15.97
S (wt.%)	0.90	2.05	0.10	1.13
K (wt.%)	1.65	2.07	1.07	0.89
Ca (wt.%)	2.51	4.23	13.64	16.67
Fe (wt.%)	2.48	4.56	1.78	2.12
Ni (µg/g)	126.4	275.1	27.1	71.2
U (µg/g)	2.6	33.5	3.8	< 0.4
Pb (µg/g)	12.9	32.5	16.4	11.5
Sr (µg/g)	275.3	182.6	884.1	494.7
Mn (µg/g)	172.9	209.2	290.8	90.0
As (µg/g)	10.3	32.4	11.9	19.7

1063
1064
1065
1066
1067

^aData are from x-ray fluorescence analysis and are reproduced from Jew et al. (*in press*).

^bUncertainty for triplicate measurements is ≤ 5%.

Table 2. Initial mineralogical composition of shale samples based on x-ray diffraction analysis^a

Mineral (wt.%) ^b	Carbonate-poor		Carbonate-rich	
	Barnett	Marcellus	Green River	Eagle Ford
Quartz	44.2	42.2	31.4	25.2
Feldspars	4.9	3.7	8.0	nd ^c
Calcite	8.2	11.6	23.2	64.5
Dolomite	nd	1.1	28.9	nd
Pyrite	2.1	6.4	nd	2.7
Analcime	nd	nd	8.5	nd
Clays	40.6	35	nd	7.6

1068
1069
1070
1071
1072
1073
1074

^aData reproduced from Jew et al. (*in press*).

^banalytical uncertainty is ≤ 15 wt.%

^cnd = not detected

1075 **Figure Captions**

1076

1077 **Figure 1.** Aqueous concentrations of (a) calcium, (b) pH, (c) iron, and (d) sulfate versus
1078 reaction time for all short-term experiments. Inset in (a) shows the percentage of total Ca
1079 remaining in the solid phase based on x-ray fluorescence spectroscopy of the initial solids
1080 and final aqueous Ca concentrations. The labels B, B2, M, EF, and GR represent the
1081 short-term Barnett, Barnett duplicate, Marcellus, Eagle Ford, and Green River
1082 experiments, respectively. Dashed lines in (c) represent calculated Fe concentrations
1083 based on measured SO_4^{2-} concentrations, assuming stoichiometric pyrite dissolution.
1084 Duplicate reactors are distinguished by filled versus unfilled symbols of the same type.
1085 Analytical error is smaller than symbol size unless otherwise shown.

1086

1087 **Figure 2.** Aqueous concentrations of (a) calcium, (b) pH, (c) iron, and (d) sulfate versus
1088 reaction time in all intermediate- and long-term experiments. Dashed and solid lines
1089 without symbols in (c) represent calculated Fe concentrations based on measured SO_4^{2-}
1090 concentrations, assuming stoichiometric pyrite dissolution. Line colors correspond to
1091 color coding for shale type as indicated in (a). Duplicate reactors are distinguished by
1092 filled versus unfilled symbols of the same type or different dash types for dashed lines.
1093 Analytical error is smaller than symbol size unless otherwise shown.

1094

1095 **Figure 3.** Silicon (a) and aluminum (b) concentrations versus reaction time in short-term
1096 experiments. Duplicate reactors are distinguished by filled versus unfilled symbols of the
1097 same type. Analytical error is smaller than symbol size unless otherwise shown. Silicon

1098 and aluminum mass balance (c) displayed as the percentage of total Si or Al remaining in
1099 the solid phase based on x-ray fluorescence spectroscopy of the initial solids and final
1100 aqueous Si and Al concentrations. Solid and striped bars represent Si and Al,
1101 respectively.

1102

1103 **Figure 4.** Saturation indices of secondary Fe(III)-bearing phases versus reaction time in
1104 the Marcellus (a) and Barnett (b) experiments of all durations. For clarity, only one of the
1105 Marcellus duplicates for the intermediate- and long-term experiments is shown. Orange,
1106 red, and black lines represent goethite [α -FeO(OH)], hematite [α -Fe₂O₃], and amorphous
1107 Fe(OH)₃, respectively. The solid grey line indicates chemical equilibrium with respect to
1108 a given solid phase (*i.e.* saturation index = 0).

1109

1110 **Figure 5.** Saturation index of calcite [CaCO₃] in all experiments. Data from the short-,
1111 intermediate-, and long-term experiments are represented by triangles, circles, and
1112 squares, respectively. Duplicate reactors are distinguished by filled versus unfilled
1113 symbols of the same type. The black dashed line indicates chemical equilibrium with
1114 respect to calcite (*i.e.* saturation index = 0).

1115

1116 **Figure 6.** Scanning electron micrographs of reacted versus unreacted shale samples.
1117 Barnett unreacted (a), Barnett reacted (b), Marcellus unreacted (c), Marcellus reacted (d),
1118 Green River unreacted (e), Green River reacted (f), Eagle Ford unreacted (g), and Eagle
1119 Ford reacted (h).

1120

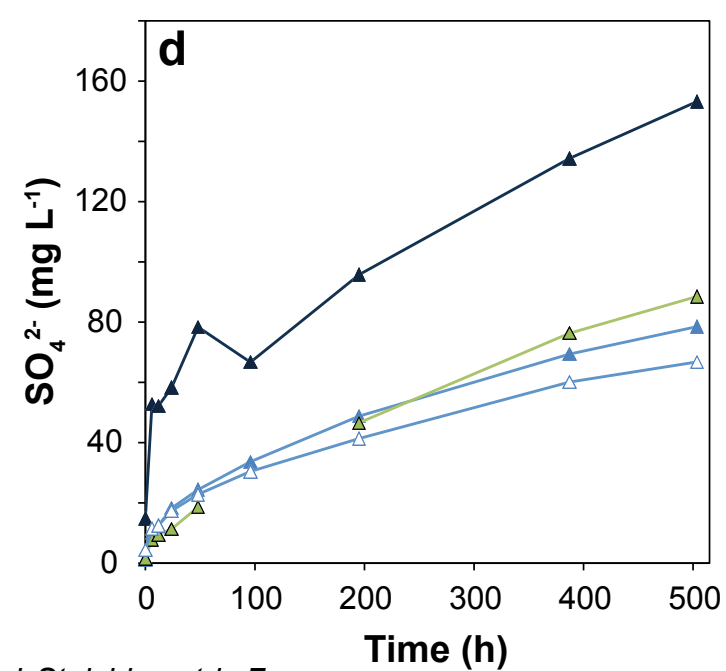
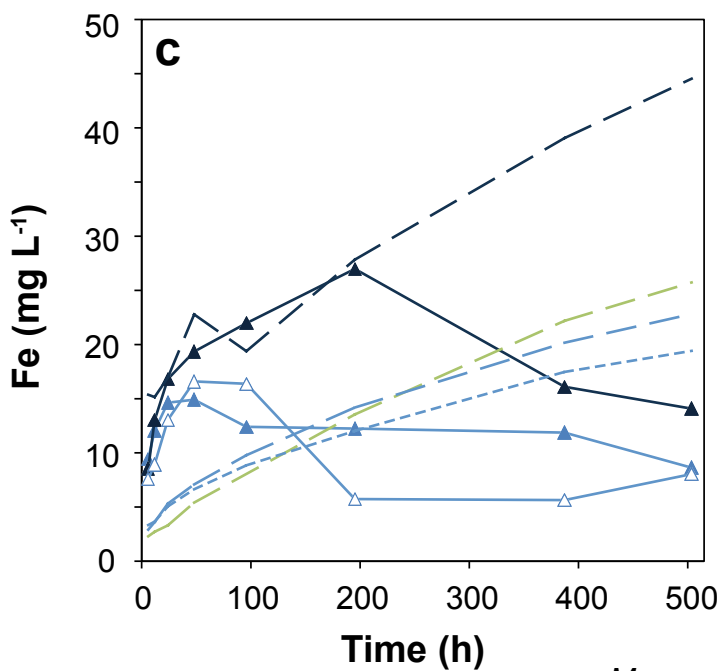
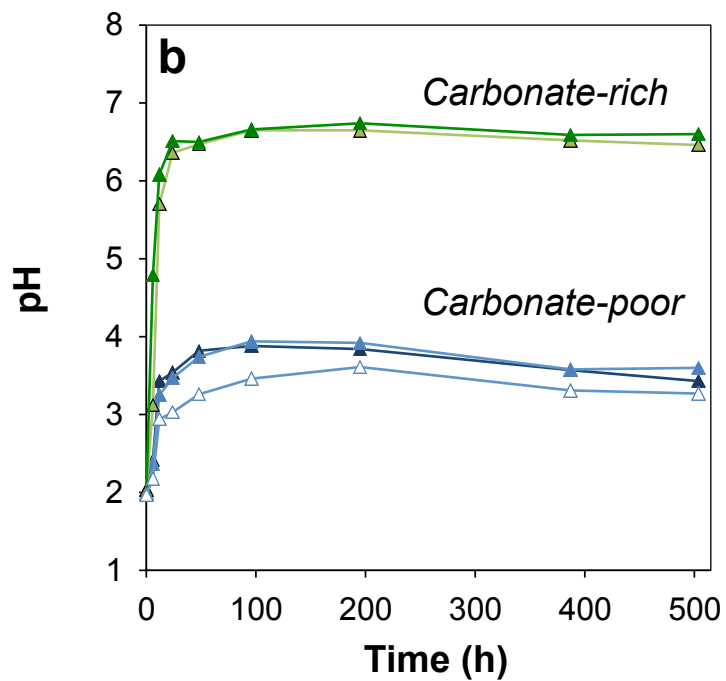
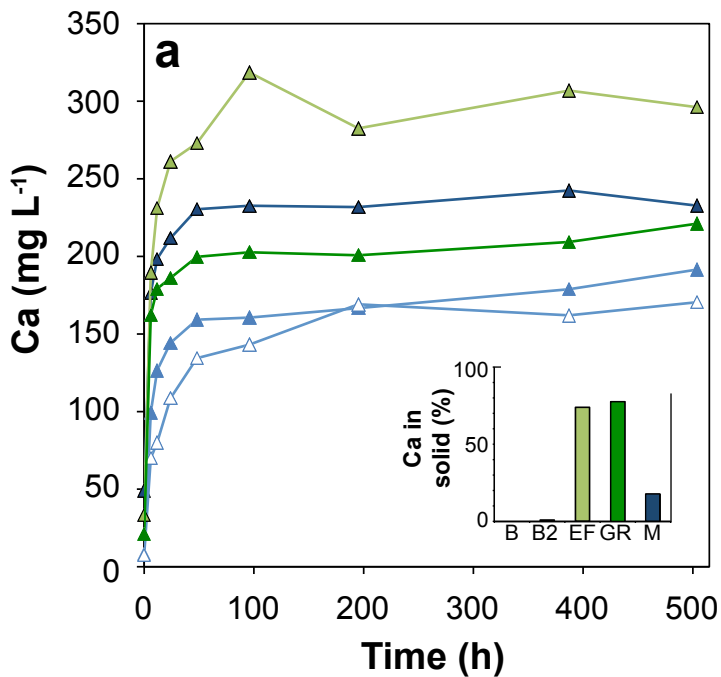
1121 **Figure 7.** Aqueous Ni concentration versus time for the Barnett, Eagle Ford (EF), and
1122 Green River (GR) reactors of all durations (a). Aqueous Ni (b), Pb (c), and U (d)
1123 concentration versus time for Marcellus reactors of all durations. Duplicate reactors are
1124 distinguished by filled versus unfilled symbols of the same type. Analytical error is
1125 smaller than symbol size unless otherwise shown.

1126

1127 **Figure 8.** Maximum measured aqueous Pb, U, and Ni concentrations versus maximum
1128 measured pH in Marcellus reactors of all durations (a). Analytical error is smaller than
1129 symbol size unless otherwise shown. Aqueous Fe to S molar ratios versus pH for all time
1130 points in Marcellus reactors of all durations (b). Duplicate reactors are distinguished by
1131 filled versus unfilled symbols of the same type.

1132

1133 **Figure 9.** Aqueous Sr concentration versus time in all reactors. Duplicate reactors are
1134 distinguished by filled versus unfilled symbols of the same type. Analytical error is
1135 smaller than symbol size unless otherwise shown.



Measured Stoichiometric Fe

Marcellus —▲—

Barnett —▲—

Barnett 2 —▲—

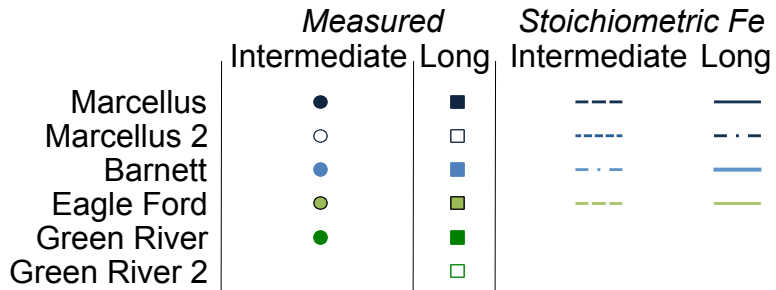
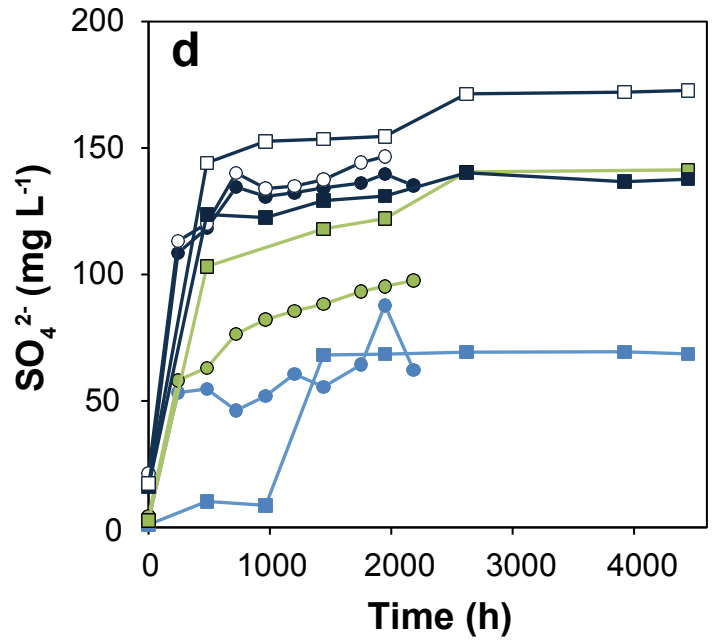
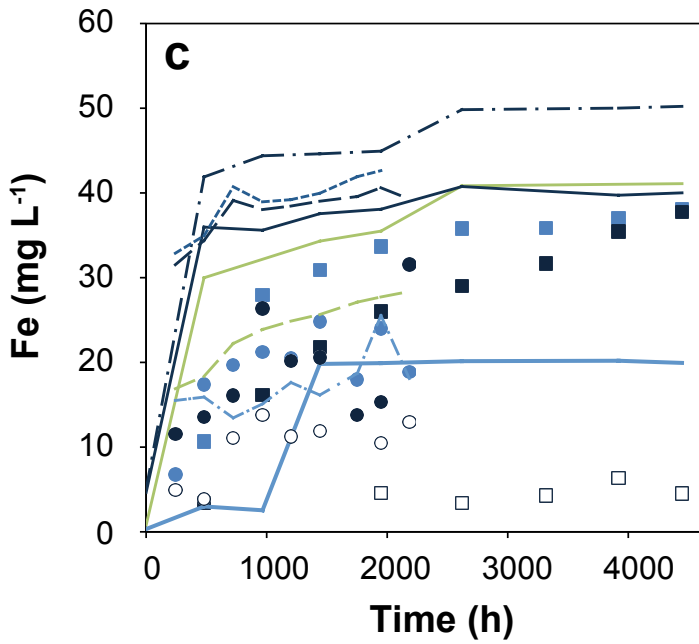
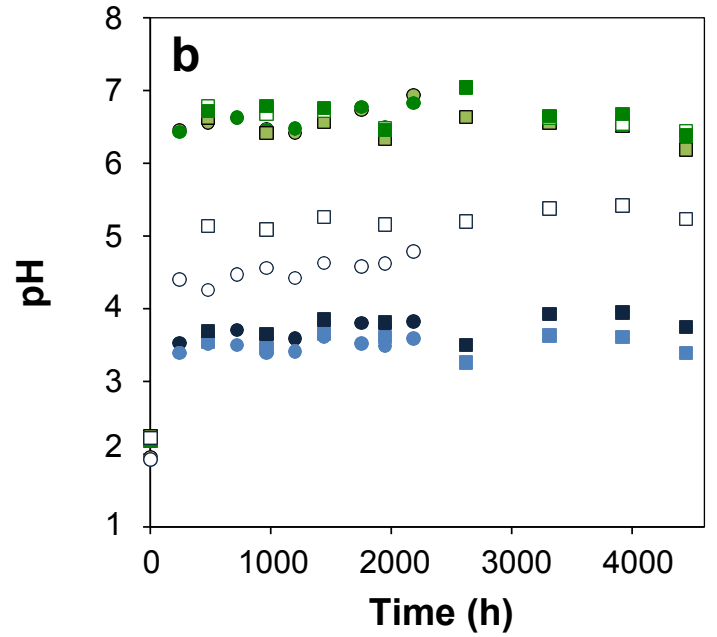
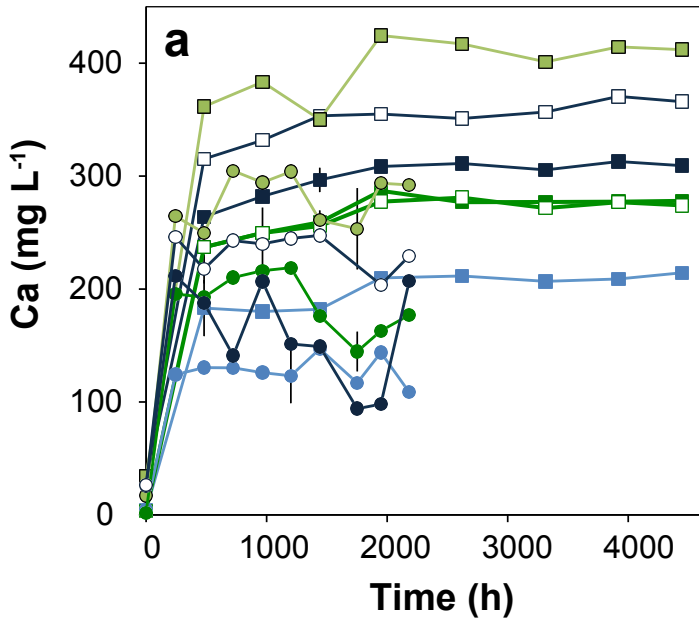
Eagle Ford —▲—

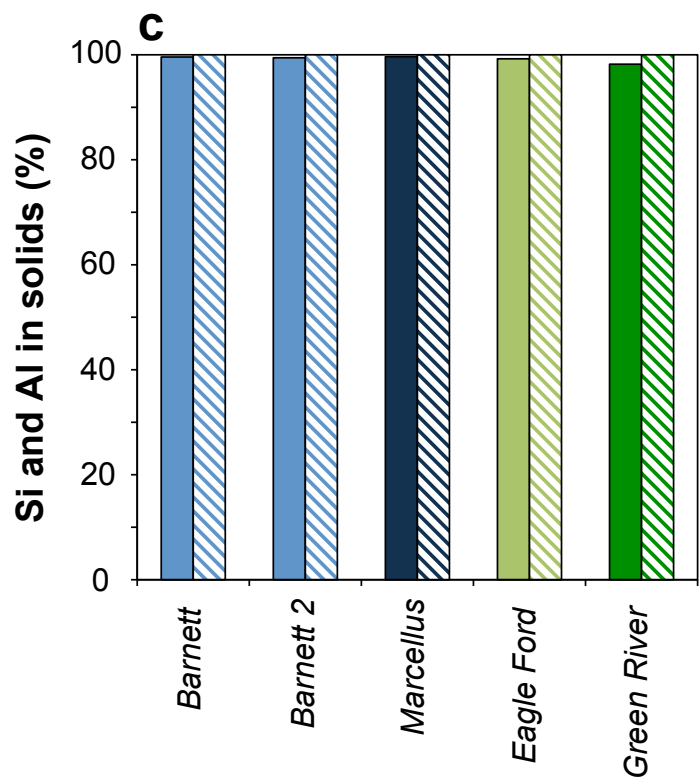
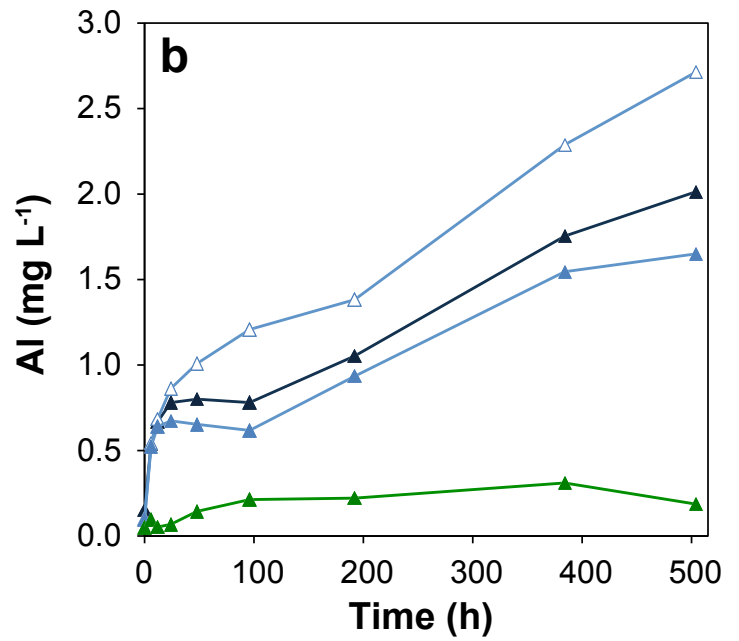
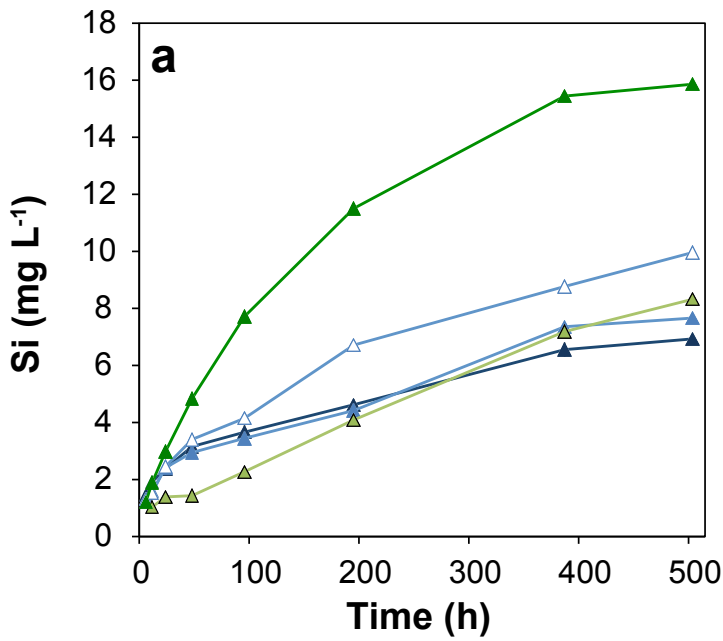
Green River —▲—

— — — — —

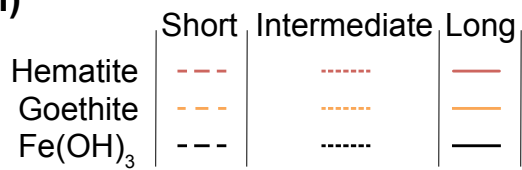
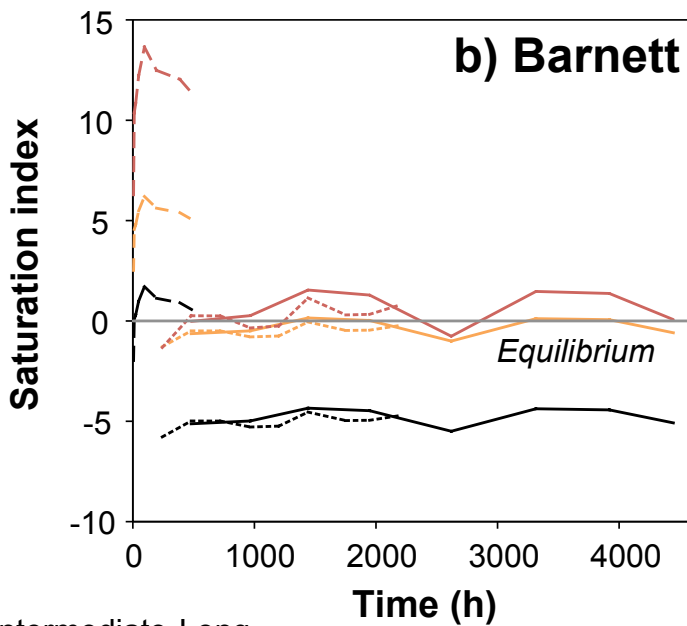
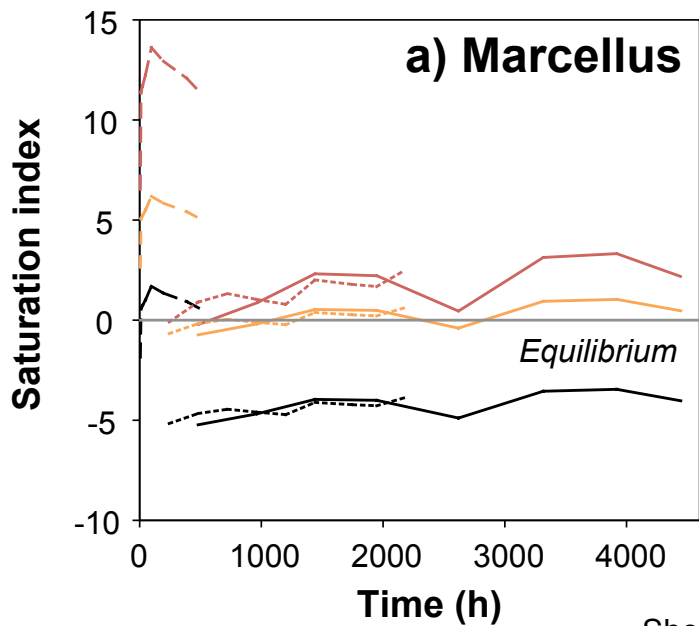
— — — — —

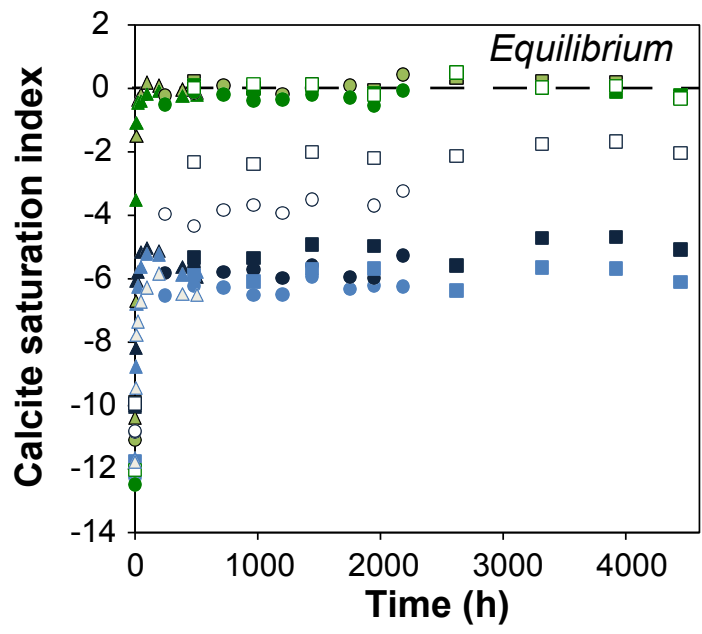
— — — — —





Marcellus ▲
 Barnett ▲
 Barnett 2 △
 Eagle Ford △
 Green River ▲





	Short	Intermediate	Long
Marcellus	▲	●	■
Marcellus 2		○	□
Barnett	▲	●	■
Barnett 2	▲	○	■
Eagle Ford	▲	●	■
Green River	▲	●	■
Green River 2			□

